



**HAL**  
open science

# Real-fluid phase transition in cavitation modelling considering dissolved non-condensable gas

Songzhi Yang, Chaouki Habchi

► **To cite this version:**

Songzhi Yang, Chaouki Habchi. Real-fluid phase transition in cavitation modelling considering dissolved non-condensable gas. *Physics of Fluids*, 2020, 32 (3), pp.032102. 10.1063/1.5140981 . hal-02553374

**HAL Id: hal-02553374**

**<https://ifp.hal.science/hal-02553374v1>**

Submitted on 5 May 2020

**HAL** is a multi-disciplinary open access archive for the deposit and dissemination of scientific research documents, whether they are published or not. The documents may come from teaching and research institutions in France or abroad, or from public or private research centers.

L'archive ouverte pluridisciplinaire **HAL**, est destinée au dépôt et à la diffusion de documents scientifiques de niveau recherche, publiés ou non, émanant des établissements d'enseignement et de recherche français ou étrangers, des laboratoires publics ou privés.

1                   Real-fluid phase transition in cavitation modelling considering  
2                   dissolved non-condensable gas

3                   Songzhi Yang (杨松枝)<sup>1,2</sup>, Chaouki Habchi\*<sup>1,2</sup>

4                   <sup>1</sup>IFP Energies Nouvelles, 1 et 4 Avenue de Bois-Préau, 92852 Rueil-Malmaison,  
5                   France

6                   <sup>2</sup>Institut Carnot IFPEN Transports Energies, 1 et 4 Avenue de Bois-Préau, 92852 Rueil-  
7                   Malmaison, France

8                   **Abstract**

9                   In this article, a fully compressible two-phase flow model combined with a multi-  
10                  component real-fluid phase equilibrium solver is proposed for the cavitation modelling.  
11                  The model is able to simulate the dissolving process of non-condensable gas through  
12                  resolving the real-fluid phase change equations. A three-dimensional cavitating nozzle  
13                  test is considered to validate the suggested model. The achieved numerical results  
14                  have been compared to available X-ray experiments. The results have confirmed that  
15                  the model can tackle the phase transition phenomena including gas dissolving and  
16                  homogeneous nucleation processes. Thus, the cavitation inception has been modelled  
17                  dynamically when the fluid crosses the phase boundary from single-phase state to two-  
18                  phase state and vice-versa. The effects of non-condensable gas on the cavitation  
19                  inception, development and unsteadiness have been particularly analysed, based on  
20                  the Large-Eddy simulations and X-ray experiments. Finally, the encountered challenges  
21                  are mentioned, aiming at providing recommendations for similar researches.

22                  **Keywords:** two-phase flow model; real fluid; dissolved gas; cavitation,  
23                  phase equilibrium

24

25

26

27

28

---

\*Corresponding author, Email: [chaouki.habchi@ifp.fr](mailto:chaouki.habchi@ifp.fr)

## 1 NOMENCLATURE

$P$	Pressure	$T$	Temperature
$P_c, T_c$	Critical pressure, temperature	$R$	Universal gas constant
$z_k,$	Molar fraction, mass fraction	$x_k, y_k$	Liquid, vapor phase mole fraction of species ( $k$ )
$Y_k$	of each species ( $k$ )	$\omega$	Vorticity
$\omega$	Acentric factor	$u$	Molar internal energy (J/mol)
$v$	Molar volume (m <sup>3</sup> /mol)	$e$	Molar internal energy (J/kg)
$\rho$	Density (kg/m <sup>3</sup> )	$Y_k$	Mass fraction of each species
$\psi_v$	Vapor molar fraction	$V_i$	Velocity (m/s)
$\alpha_g, \alpha_l$	Volume fraction of gas, liquid	$C_{s,g}, C_{s,l}$	Speed of sound in the gas phase, liquid phase (m/s)
$C_s$	Speed of sound (m/s)	$k_{i,j}$ / BIP	Binary interaction parameter
$\alpha_p \rho_{p,k}$	Specific density of component $k$ in phase $p$ (kg/m <sup>3</sup> )	$Pr$	Prandtl number
$M_w$	Molar weight (kg/mol)		
$\mu$	Dynamic viscosity (kg/(m*s))		
<b>Superscripts</b>			
$n$	Numerical values in current time step	,	Temporary numerical values during the iteration process
$L, T$	Laminar/turbulent	C	Numerical results after the flow solver or Phase C
<b>Subscripts</b>			
$k$	Species index	$g$	Gas phase
$l$	Liquid phase	$p$	Phase index
<b>Abbreviations</b>			
PR EoS	Peng-Robinson equation of state	TP flash	Isothermal-Isobaric flash
UV flash	Isoenergetic-Isochoric flash	HTHP	High temperature high pressure
DIM	Diffused interface model	HEM	Homogeneous Equilibrium Model
HRM	Homogeneous Relaxation Model	VOF	Volume of fluid
LS	Level-set	EoS	Equation of state
3D	Three-dimensional		

2

## 1           **1. Introduction**

2           Cavitation is the development of vapor bubbles in a flowing liquid. It is triggered as  
3           the local static pressure drops to the fluid saturated value. This phenomenon may  
4           happen in hydraulic devices such as hydro-turbines, propellers, pumps or fuel injectors  
5           [1]–[4]. This study is mainly focused on but not limited to cavitation in injectors. For  
6           internal combustion engines, the important effects of in-nozzle cavitation on the fluid  
7           velocity, discharge coefficient, as well as on the ensuing fuel-air mixing, engine  
8           performance and emission pollutants have been widely recognized and studied [5]–  
9           [9].

10          The most direct cavitation investigation strategy is through experimental observations  
11          which is generally based on the transparent optical configurations (nozzles, chambers,  
12          etc). The progress of experimental techniques, from the qualitative laser-sheet and  
13          shadowgraph techniques [10], [11], to the quantitative X-ray computed tomography  
14          techniques [12], [13], and even more recent X-ray radiography [14], [15], have  
15          significantly facilitated the observations of the in-nozzle cavitation. Meanwhile,  
16          cavitation modelling and simulation also play a key complementary role in the  
17          verification of experimental results, which is also the main strategy adopted in this  
18          study.

19          As for the modelling of dispersed phase (bubble or droplet), the numerical models  
20          involved can be classified into two categories: the Eulerian continuum approach and  
21          the Lagrangian discrete approach. The first approach may be a single-fluid  
22          homogeneous model or a multi-fluid model. The widely employed single-fluid  
23          Homogeneous Equilibrium Model (HEM) [8], [16]–[18] and Homogeneous Relaxation  
24          Model (HRM) [19], [20] have demonstrated excellent performance in predicting  
25          cavitating flows. More complicated two-fluid model can describe the liquid and vapor  
26          phase simultaneously with individual mass, momentum and energy in each cell as  
27          studied in [21]–[23]. In the alternative discrete Lagrangian approach, the vapor phase  
28          is usually treated as the dispersed phase or nuclei state with the prescribed diameter  
29          and number distributions, as demonstrated in previous works [13], [24], [25].

30          Besides, depending on the method of locating the interface, the interface tracking  
31          models such as Level-Set (LS) and VOF (fluid volume) [9], [26], or the diffuse interface  
32          model (DIM) [21], [27], may be used.

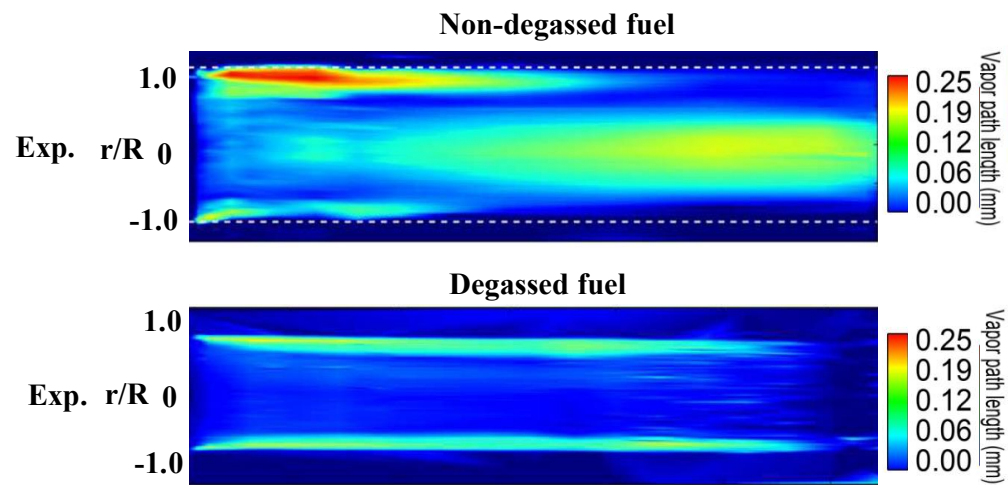
33          In current study, the continuous single-fluid two-phase flow diffused interface model  
34          (DIM) is adopted. As a thermodynamic closure for the flow model, a real fluid cubic  
35          equation of state (EoS) is employed in order to investigate the effect of real flow  
36          properties on phase transition in cavitation modelling with the consideration of  
37          dissolved non-condensable gas. In recent years, the real fluid EoS has been widely

This is the author's peer reviewed, accepted manuscript. However, the online version of record will be different from this version once it has been copyedited and typeset.

PLEASE CITE THIS ARTICLE AS DOI:10.1063/1.5140981

1 employed in the two-phase flow simulation, especially for the high pressure injection  
2 [28]–[30]. However, the scenario of cavitation simulation with real fluid equation of  
3 state is still extremely scarce for its high thermodynamically and numerical  
4 complexities. Indeed, introducing the real fluid EoS into the cavitation modelling  
5 enables us to take into account more real and practical physical phenomena, for  
6 example the process of gas dissolving and relief from liquid. The widely used EoS like  
7 Stiffened-gas EoS [31]–[35], Tait EoS [36] have shown excellent performance in the  
8 cavitation modelling in previous studies. Nevertheless, the above mentioned EoSs are  
9 not able to address the aforementioned gas dissolving physics, especially bubbles  
10 inception. As a matter of fact, cavitation bubbles also contain non-condensable gas  
11 that diffuses into them from the liquid where it is present as dissolved gas. Therefore,  
12 both liquid and gas phases are multi-component when using real fluid  
13 thermodynamics and Vapor-Liquid-Equilibrium (VLE). Recently, Yu, et al. [37] have  
14 developed a multiphase compressible model in which the vapor, liquid and non-  
15 condensable gas phase are simultaneously considered. However, the real fluid EoS has  
16 been applied only for the gas phase to simulate the cavitation and high-pressure diesel  
17 sprays. Thus the gas dissolving process is still neglected in their model. On the other  
18 hand, the current model avoids the cumbersome process of prescribing the empirical  
19 coefficients for the calculation of cavitation and collapse terms. The validations of the  
20 current model applied to flash boiling cases and high temperature, high pressure  
21 (HTHP) diesel injection process can be found in our recent studies [30], [38]. One  
22 noting point about the employment of cubic EoSs series in the multiphase flow  
23 equation is the risks of losing hyperbolicity when entering the spinodal region as  
24 discussed by many researchers [27], [32], [39], [40]. However, this risk can be  
25 prevented through adopting the composite EoS in which liquid flow and gas flow are  
26 described with its independent EoS instead of a mixture EoS [38]. Thus, the validity of  
27 the speed of sound in the two phase region is sustained by the mixing of each  
28 individual positive speed of sound in the liquid phase and vapor phase through the  
29 Wood formula [41]. This strategy is adopted in current study.

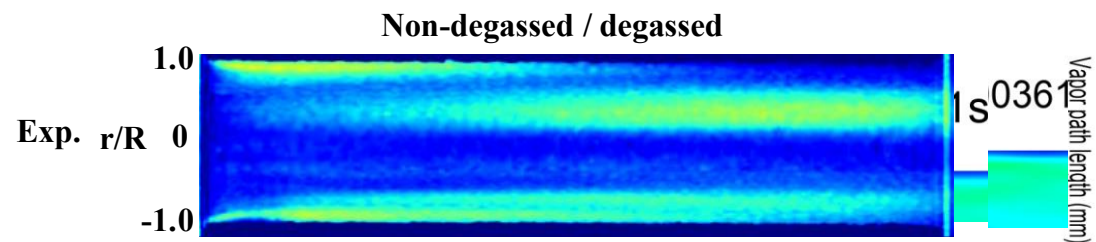
30 The research interest in this paper stems from the recent X-ray radiography  
31 experiments [42], [43] in which an extra cavitation cloud was observed in the center  
32 line of the orifice where the pressure is slightly higher than the saturation value of the  
33 fuel as demonstrated in Figure 1 (non-degassed fuel represents the standard fuel).  
34 This cavitation cloud appeared in the center line has diminished significantly as  
35 decreasing the initial non-condensable gas amount in the fuel as illustrated in Figure  
36 1 (degassed fuel).



1  
2  
3  
4  
5  
6  
7  
8

Figure 1 Contour plots of the time-averaged void fraction from the X-ray radiography measurements. The experiment is conducted with a plastic nozzle. These experimental images are republished with permission of Begell house, from 'Duke, Daniel J., et al. "X-Ray Radiography Measurements of Cavitating Nozzle Flow." *Atomization & Sprays* 23.9(2013):841-860.', permission conveyed through Copyright Clearance Center, Inc. The configuration of the geometry is illustrated in Figure 6.

9 The ensuing numerical results from Battistoni et al. [20] with the HRM model again  
10 confirm that the void zones are significantly decreased in the center line as the non-  
11 condensable gas amount is reduced in the fluid. However, the latest X-ray radiography  
12 experimental measurements from Duke, et al. [15] (Figure 2) about the effect of  
13 dissolved gas on cavitation have questioned the previous experimental and numerical  
14 findings.



15  
16  
17  
18  
19  
20  
21  
22

Figure 2 Contour plots of the time-averaged void fraction from the X-ray radiography measurements. The experiment is conducted with the beryllium alloy nozzle. Only one image is displayed since very similar results are obtained using the non-degassed (standard) fuel and degassed fuel. The experiment image is reprinted with permission of SAGE Publications, Ltd, from 'Duke, Daniel J., et al. "X-Ray Radiography of Cavitation in a Beryllium Alloy Nozzle." *International Journal of Engine Research*, vol. 18, no. 1–2, Feb. 2017, pp. 39–50' copyright ©2020. The configuration of the geometry is illustrated in Figure 6.

23 They have attributed the void zone in the center line appeared in the earlier  
24 experiment [42] (Figure 1, non-degassed case) to the existence of defects on the wall  
25 of plastic nozzle, which acts as potential heterogeneous nucleation sites. In contrast,

1 fewer defects are detected in the beryllium nozzle surface used more recently in [15],  
2 leading to very similar experimental averaged results using the non-degassed  
3 (standard) and degassed fuels (Figure 2). The significant deviations between these two  
4 experimental results (Figure 1 vs. Figure 2) have brought in more uncertainty about  
5 the understanding of the effect of dissolved gas on cavitation, which thereby has  
6 motivated the current numerical study.

7 There are also abundant studies concerning the effect of non-condensable gas on  
8 spray pattern and engine efficiency [44]–[48]. However, the investigations of the  
9 effect of non-condensable gas on cavitation are still limited. Battistoni et al. [20] has  
10 employed the HRM model to simulate the in-nozzle cavitation in which the non-  
11 condensable gas term is treated as the third phase in addition to the liquid and vapor  
12 phases. One noting point is that the non-condensable gas phase in their model is seen  
13 as free gas which cannot be dissolved into the liquid and is therefore not participating  
14 in the phase change process. Whilst with current real fluid phase equilibrium model  
15 proposed below, the non-condensable gas can be dissolved into the liquid and is  
16 indeed able to experience phase transition, which may promote the fuel evaporation.

17 As a matter of fact, once the phase transition is triggered, this denotes the non-  
18 condensable gas has been through the nucleation process, first and before the fuel as  
19 it is generally the most volatile.

20 In the work of Zhang et al. [49], they demonstrated experimentally that the dissolved  
21 oxygen has minor effect on the length of cavitation in a Venturi tube. Amini et al. [50]  
22 investigate the incipience and completion thresholds of tip vortex cavitation in a  
23 hydrofoil with varied amount of dissolved gas through experimental observations.  
24 They found that the tip vortex cavitation incepts at lower pressure as the dissolved  
25 amount gas is reduced and disappears at much higher pressure in the fully saturated  
26 water. Giresan and Pandit [51] have used the diffusion limited model to study the  
27 influence of the CO<sub>2</sub> and Argon (Ar) mixture on the cavitation and find that the bubble  
28 grows larger and the intensity of collapse decreases as CO<sub>2</sub> composition is increased.

29 In general, it is found that the studies of the non-condensable gas are closely linked  
30 with the nucleation rate, cavity generation rate, bubble collapse intensity, surface  
31 tension and other chemical properties.

32 The research here is devoted to shedding some light on the understanding of the  
33 effect of dissolved gas on the in-nozzle cavitation phenomena using a real fluid EoS.  
34 The main difference with previous models lies in the method of dealing with gaseous  
35 and vaporous cavitation. In current study, both cavitation regimes can be simulated  
36 with the thermodynamics equilibrium model [52]. However, the non-condensable gas  
37 part involved in previous cavitation modelling [19], [20] has been treated as free gas  
38 instead of dissolved gas. In fact, in the current model described below, the dissolved

1 gas is modelled as a part of the liquid phase and its dissolution (or separation) from  
 2 liquid is closely linked with the homogeneous nucleation phenomenon.  
 3 This paper has been organized as followings: first, the mathematics descriptions about  
 4 the two-phase flow model and thermodynamics solver are briefly recalled. More  
 5 detailed descriptions can be found in our previous work [38][53]. Next, the numerical  
 6 results of the three-dimensional (3D) simulations of a real size cavitating nozzle are  
 7 reported along with a detailed analysis. The conclusions part describes the main  
 8 findings and challenges of the current work.

## 9 2. Mathematical model

### 10 2.1 Fully Compressible two-phase flow DIM model

11 The governing equation adopted in current study is a fully compressible  
 12 multicomponent two-phase flow four-equation model. This system is obtained from  
 13 the classical two-phase flow non-equilibrium 7-Equation model [54] with the  
 14 assumption of mechanical and thermal equilibrium. As formulated in the following  
 15 Eqs.(2.1)-(2.4), the four-equation model includes the mass balance equations for  
 16 different species (index:  $k$ ) in the gas (index:  $g$ ) and liquid (index:  $l$ ) phases (Eqs.(2.1)-  
 17 (2.2)), mixture momentum (Eq.(2.3)), and mixture specific internal energy (Eq.(2.4)),  
 18 respectively.

$$19 \quad \frac{\partial \alpha_l \rho_{l,k}}{\partial t} + \frac{\partial \alpha_l \rho_{l,k} V_i}{\partial x_j} = \dot{m}_{l,k} \quad (2.1)$$

$$\frac{\partial \alpha_g \rho_{g,k}}{\partial t} + \frac{\partial \alpha_g \rho_{g,k} V_i}{\partial x_j} = \dot{m}_{g,k} \quad (2.2)$$

$$\frac{\partial \rho V_i}{\partial t} + \frac{\partial \rho V_i V_j}{\partial x_i} = \frac{\partial P}{\partial x_i} + \frac{\partial \tau_{ij}^{L,T}}{\partial x_i} \quad (2.3)$$

$$\frac{\partial \rho e}{\partial t} + \frac{\partial \rho e V_i}{\partial x_i} = -P \frac{\partial V_i}{\partial x_i} - \frac{\partial q_i^{L,T}}{\partial x_i} + \tau_{ij}^{L,T} \frac{\partial V_i}{\partial x_j} \quad (2.4)$$

20  
 21 The right hand side (RHS) terms of  $\dot{m}_{l,k}$  and  $\dot{m}_{g,k}$  are mass exchanging rate in the  
 22 liquid and vapor phases, respectively, restricted by  $\dot{m}_{l,k} + \dot{m}_{g,k} = 0$ .  $\tau_{ij}^{L,T}$  is the shear  
 23 stress tensor covering the laminar ( $L$ ) and turbulent ( $T$ ) contributions, formulated as  
 24  $\tau_{ij}^{L,T} = \tau_{ij}^L + K_0 \tau_{ij}^T$  with  $K_0 = 1$  for turbulent flows. As described in our previous  
 25 studies [21], [38], a standard Boussinesq approximation is used for the modelling of



1  $\tau_{ij}^{L,T}$  in which the turbulent viscosity is given by the simple subgrid-scale Smagorinsky  
 2 model. Whereas, the laminar viscosity is computed from Chung's equation, referring  
 3 to [55], [56]. In Eq.(2.4),  $e$  represents the specific internal energy;  $q_i^{L,T}$  is the heat  
 4 conduction flux, modelled as  $q_i^{L,T} = -\lambda \frac{\partial T}{\partial x_i}$  based on Fourier's law. The heat  
 5 conduction coefficient  $\lambda$  contains the laminar and turbulent contributions. The  
 6 laminar contribution is computed from Chung's correlation and the turbulent one is  
 7 estimated with the constant Prandtl number ( $Pr_t = 0.9$ ).  $\alpha_p$  denotes the volume  
 8 fraction of phase  $p$  which is computed in the phase equilibrium solver along with  $\dot{m}_{p,k}$ .  
 9 One salient point about the current model lies in the consideration of the nucleation  
 10 and dissolving process of the non-condensable gas which is realized with the real-fluid  
 11 phase equilibrium model. The liquid phase is indeed a multi-component system  
 12 including both fuel and dissolved non-condensable gas. In most previous cavitation  
 13 models, only the gas phase is usually considered as multi-component, and the liquid  
 14 phase is assumed as single component [9], [20]. In current equation system, the mass  
 15 transferring between the liquid and gas phase is computed in Vapor-Liquid-  
 16 Equilibrium (VLE) solver for each component (see Section 2.2.2). Thereby the number  
 17 of mass transport equation is  $2 * N$  ( $N$  denotes the number of species). The  
 18 employment of real fluid EoS in each phase also facilitates the consideration of  
 19 compressibility and other related physics, especially for the pure liquid phase and two-  
 20 phase mixtures.

## 22 **2.2 Real fluid phase equilibrium solver**

### 23 **2.2.1 Equation of state**

24 To realize the free dissolving and dissolution of the non-condensable gas, as well as  
 25 considering the thermal effect during cavitation, a non-linear real fluid equation of  
 26 state has been selected in current study. With the ideal compromise of computational  
 27 efficiency and accuracy, Peng Robinson (PR) EoS (Eq.(2.5)) is chosen to describe the  
 28 relation between  $P$ ,  $v$  and  $T$ . As aforementioned, the studies of cavitation modelling  
 29 with real fluid EoS are still limited. For instance, Yu et al. [37] has recently applied the  
 30 PR EoS to take into account the thermal effects for in-nozzle cavitation modelling  
 31 under high injection pressure conditions. However, the dissolved gas effect is still  
 32 neglected in their study. In the current modelling approach, both phases (the liquid  
 33 and gas phases) are described with the PR EoS (Eq.(2.5)) linked through the phase  
 34 equilibrium assumption. For each phase the mixing of different species is realized by  
 35 the van der Waals mixing rule (Eq.(2.6)).  
 36

$$P = \frac{RT}{v-b} - \frac{a(T)}{v(v+b) + b(v-b)} \quad (2.5)$$

1 Where,  $a(T) = 0.45724 \frac{R^2 T_c^2}{P_c} \alpha(T)$ ,  $b = 0.07780 \frac{RT_c}{P_c}$ ,  $\alpha(T) = (1 + m(1 - \sqrt{T_r}))^2$   
 $m = 0.37464 + 1.5422\omega - 0.26992\omega^2$

2  $R$  denotes the universal gas constant.  $P_c$  and  $T_c$  represent the critical pressure and  
 3 temperature values for single component and  $\omega$  denotes the acentric factor.  
 4 van der Waals mixture rules are formulated as follows,

$$a = \sum \sum x_i * x_j * a_{ij}$$

$$a_{ij} = (1 - k_{ij})(a_i * a_j)^{0.5} \quad (2.6)$$

$$b = \sum x_i * b_i$$

6  $x_i$  is the molar fraction of each component.  $k_{ij}$  denotes the binary interaction  
 7 parameter which is generally fitted based on the experimental data.

### 8 2.2.2 Phase change model

9 The critical phase change phenomena (evaporation, condensation) during the  
 10 cavitation modelling are realized with a multicomponent vapor-liquid equilibrium (VLE)  
 11 model which is constructed based on the assumption that liquid and vapor phase  
 12 reach equilibrium instantaneously within each simulation time step. No constraint is  
 13 set for the time-scale of relaxation to equilibrium with current model compared to the  
 14 Homogeneous Relaxation Model (HRM) [14]. All the fluid states including the pure  
 15 liquid phase, pure vapor phase and the vapor-liquid coexisting state can be  
 16 dynamically simulated using the proposed model.

17 The right hand side terms ( $\dot{m}_{l,k}$ ,  $\dot{m}_{g,k}$ ) calculation and closure of the flow system  
 18 (Eqs.(2.1) -(2.4)) are realized by building the relation between internal energy ( $e$ ),  
 19 density ( $\rho$ ), mass fraction ( $Y_k$ ) and pressure ( $P$ ), temperature ( $T$ ), known as the UV  
 20 flash process [57][38]. First, with the direct unit transformation, molar internal energy  
 21 ( $u$ ) and molar volume ( $v$ ) can be obtained directly from ( $e$ ) and ( $\rho$ ) using molar weight  
 22  $M_w$ , as shown in Eq.(2.7). The molar internal energy ( $u$ ) is computed with the ideal gas  
 23 part ( $u_0$ ) and the departure part ( $u_d$ ) (given by Eq.(2.8)). The ideal gas internal energy  
 24 is obtained with the empirical coefficient correction equation referred to [58]. The  
 25 departure function is formulated as Eq.(2.9) according to the PR EoS. The density ( $\rho$ )  
 26 or specific volume ( $v$ ) is computed directly by solving the cubic equation [59]. Unlike  
 27 the explicit relation between internal energy ( $u$ ) and temperature ( $T$ ) as in SG EoS [32],  
 28 [33], an iterative algorithm is necessary to find  $P, T$  from  $u, v$  and  $z_k$  (molar fraction  
 29 of the species) with the cubic EoS. Before initiating the UV flash iteration process, the  
 30 initial molar fraction of species ( $z_k^c$ ) in the two-phase mixture, the quasi-steady or non-  
 31 equilibrium phase compositions (liquid phase and vapor phase:  $x_k^c, y_k^c$ ) and the vapor  
 32 mole fraction ( $\psi_k^c$ ) in the liquid-vapor mixture can be computed from the specific  
 33 densities ( $\alpha_p^c \rho_{p,k}^c$ ) by using Eqs.(2.10)-(2.11). Here, the superscript  $c$  denotes the  
 34 values obtained from the flow solver at the end of Phase C (see Section 2.2.3 and

1 particularly Figure 3).Then, the solving procedures are continued with the  
 2 determination of flow state as shown in the algorithm summarized in Table 1. Since  
 3 the  $(P^{n+1}, T^{n+1})$  for next cycle are not known as a prior, the  $(P^n, T^n)$  from previous  
 4 cycle are used as the initial guess to perform the stability test [38], [53]. This method  
 5 is valid based on the fact that the time step is small between two flow solver cycles.  
 6 Once the flow state is ascertained, an iterative procedure is necessary to obtain the  
 7 final  $(P^{n+1}, T^{n+1})$ . During the iteration, the molar internal energy and molar volume  
 8 (denoted  $u_{mix}$  and  $v_{mix}$ ) are updated with the properties of each phase Eq.(2.12).  
 9 One noting point is that in the case of single phase, the phase composition  $x_k^{n+1}, y_k^{n+1}$   
 10 and molar vapor fraction  $\psi_v^{n+1}$  are assumed to be the same as the values of  $x'_k, y'_k$   
 11 and  $\psi'_v$  obtained by the flow solver. Generally, the opposed phase in the single-phase  
 12 situation is seen as the trifle phase. Eventually, the new specific density  $\alpha_p^{n+1}\rho_{p,k}^{n+1}$  are  
 13 calculated with Eq.(2.13) using the volume fraction ( $\alpha_p^{n+1}$ ) and the final molar volume  
 14 of species in each phase obtained from PR EoS. The speed of sound ( $Cs^{n+1}$ ) is then  
 15 computed with the Wood formula written as Eq.(2.14). Since the mixture speed of  
 16 sound in the two-phase state is computed with the mixing of the independent speed  
 17 of sound in each phase, this can effectively avoid the unphysical negative speed of  
 18 sound. Thereby, the hyperbolicity of the flow balance equation system (Eq.(2.1)-(2.4))  
 19 is thus ensured, as discussed in [38]. More detailed descriptions about the thermal  
 20 solver can be found in recent publications [38], [53].  
 21

$$u = e * M_w, v = \frac{M_w}{\rho} \quad (2.7)$$

$$\mathbf{u} = \mathbf{u}_d + \mathbf{u}_0 \quad (2.8)$$

$$\mathbf{u}_d = \frac{T \frac{da}{dT} - a}{2\sqrt{2}b} \ln\left(\frac{v + (1 + \sqrt{2})b}{v + (1 - \sqrt{2})b}\right) \quad (2.9)$$

22  
23

**Table 1 Algorithm of UV flash**

<b>Algorithm 1</b> Update $P^{n+1}, T^{n+1}, Cs^{n+1}, \alpha_p^{n+1}\rho_{p,k}^{n+1}$ from $e^c, \rho^c, \alpha_p^c\rho_{p,k}^c, P^n, T^n$
<b>STEP 0</b> Compute $u^c, v^c, \psi_v^c, z_k^c, x_k^c, y_k^c$ from $e^c, \rho^c, \alpha_p^c\rho_{p,k}^c$ using Eqs.(2.7), (2.10)-(2.11)
<b>STEP 1</b> Verify Initial flow state based on $(u^c, v^c, z_k^c)$ and $(P^n, T^n, z_k^c)$ through stability test.
<b>STEP 2</b> If the flow state is stable as single phase, a direct iteratively searching for the updated $(P', T')$ with Newton algorithm based on PR EoS is performed with the initial quasi-steady phase composition $(x_k^c, y_k^c)$ and vapor fraction $(\psi_v^c)$ . Here assign $x'_k = x_k^c, y'_k = y_k^c, \psi'_v = \psi_v^c$ .
<b>STEP 3</b> If the flow state is unstable, an iteratively searching for the updated $P', T'$ with Newton algorithm is performed with the continuous updating of phase composition $(x'_k, y'_k)$ and vapor fraction $(\psi'_v)$ based on phase split computation in the inner loop. ( see Ref.[38] for the involved algorithm)
<b>STEP 4</b> Update $P^{n+1}, T^{n+1}, Cs^{n+1}, \alpha_p^{n+1}\rho_{p,k}^{n+1}$ from $x'_k, y'_k, \psi'_v$ by using Eqs.(2.13)-(2.14) and Eq.(2.5)

24

$$\mathbf{z}_k = \frac{(\sum_p \alpha_p \rho_{p,k}) M_{w_{mix}}}{(\sum_{p,k} \alpha_p \rho_{p,k}) M_{w_k}}, \mathbf{Y}_k = \frac{(\sum_p \alpha_p \rho_{p,k})}{(\sum_{p,k} \alpha_p \rho_{p,k})} \quad (2.10)$$

$$\mathbf{x}_k = \frac{\alpha_l \rho_{l,k} M_{w_l}}{\sum_k (\alpha_l \rho_{l,k}) M_{w_k}}, \mathbf{y}_k = \frac{\alpha_g \rho_{g,k} M_{w_g}}{\sum_k (\alpha_g \rho_{g,k}) M_{w_k}}, \psi_v = \frac{(\sum_k \alpha_g \rho_{g,k}) M_{w_{mix}}}{\rho M_{w_g}} \quad (2.11)$$

1  
2  
3  
4  
5

$M_{w_k}$  denotes the molar weight of species ( $k$ ).  $M_{w_g}$ ,  $M_{w_l}$  represent the average molar weight of gas phase and liquid phase, respectively.  $\rho_{p,k}$  represents the partial density of species  $k$  in phase  $p$ .

$$\mathbf{u}_{mix} = \psi_v * \mathbf{u}_g + (1 - \psi_v) * \mathbf{u}_l \quad (2.12)$$

$$v_{mix} = \psi_v * v_g + (1 - \psi_v) * v_l$$

$$\rho = \frac{M_w}{v}, \rho = \alpha_g \rho_g + \alpha_l \rho_l, \quad (2.13)$$

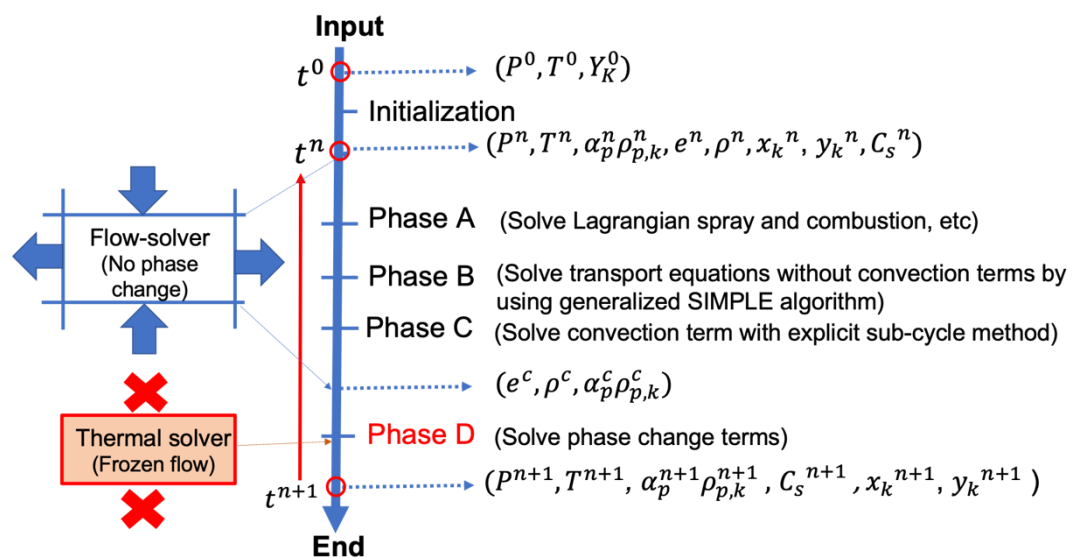
$$\alpha_g = \psi_v * \frac{v_g}{\psi_v v_g + (1 - \psi_v) v_l}, \text{ with } \alpha_l = 1 - \alpha_g$$

$$\frac{1}{\rho_{mix} C_{s,mix}^2} = \frac{\alpha_g}{\rho_g C_{s,g}^2} + \frac{\alpha_l}{\rho_l C_{s,l}^2} \quad (2.14)$$

### 6      2.2.3      Coupling of flow solver with phase change model

7      In this Section, the coupling procedure between the thermodynamics solver and the  
8      flow solver is elucidated to enhance the understanding of the main implementation  
9      stages. In IFP-C3D [60], the transport equations (mass, momentum, energy balance  
10      equations) are solved sequentially from Phase A, Phase B, Phase C Phase D based on  
11      a time-splitting numerical scheme, as illustrated in Figure 3. The solver includes the  
12      flow solver and thermodynamics solver. The flow solver covers three stages namely,  
13      Phase A, Phase B and Phase C. First, after the initialization ( $t = t^0$ ), the contribution  
14      of possible Lagrangian spray and combustion source terms may be computed in Phase  
15      A. Therefore, Phase A stage is not pertinent for the current flow system (Eqs.(2.1) -  
16      (2.4)). In the following Phase B stage, usually called ‘‘Lagrangian phase’’, the Navier-  
17      Stokes equations are solved without the convection terms and the pressure,  
18      temperature and velocity are updated implicitly with the SIMPLE numerical  
19      scheme[61], including a BICGSTAB and SOR preconditioners [60]. Then, the grid cell  
20      boundaries are mapped back to their original position (in the absence of wall  
21      movement) in Phase C (also called ‘‘Eulerian stage’’). The transport variables including  
22      mass, energy and momentum from Phase B are updated in Phase C using a quasi-  
23      second order upwind (QSOU) explicit numerical scheme. The Minmod slope limiter is  
24      used for scalar fluxes, and Van Leer slope limiter is used for momentum fluxes (see  
25      [60]). No phase change is considered in these three stages. The thermodynamic solver  
26      is implemented in the final stage, Phase D. With the known internal energy ( $e^c$ ),  
27      density ( $\rho^c$ ) and specific density ( $\alpha_p^c \rho_{p,k}^c$ ) from phase C, the new temperature ( $T^{n+1}$ ),

1 pressure ( $P^{n+1}$ ), phase compositions ( $x_k^{n+1}, y_k^{n+1}$ ) and speed of sound ( $C_s^{n+1}$ ) need  
 2 to be calculated for ending the current time-step (or cycle). This procedure is  
 3 attributed to the phase change model as described in Section 2.2.2. In phase D, the  
 4 occurred evaporation or condensation phenomenon corresponds to the generation  
 5 and collapse of bubbles during cavitation. One noting point is that there is no fluid  
 6 flowing in or out of Phase D which means the flow is frozen in this stage. In fact, the  
 7 phase equilibrium solver based on PR EoS has corresponded to the relaxation of  
 8 pressure, temperature and the Gibbs energy terms in the original 7-Equation model  
 9 [21]. Since the liquid and gas phases are both resolved as multicomponent system, the  
 10 involved gas phase or dissolved gas in the liquid phase constitutes the main physical  
 11 novelty compared to previous researches using SG-EoS for instance [21], [62], [63].  
 12



13

14

Figure 3 Illustration of coupling between the thermodynamic solver and flow solver in IFP-C3D

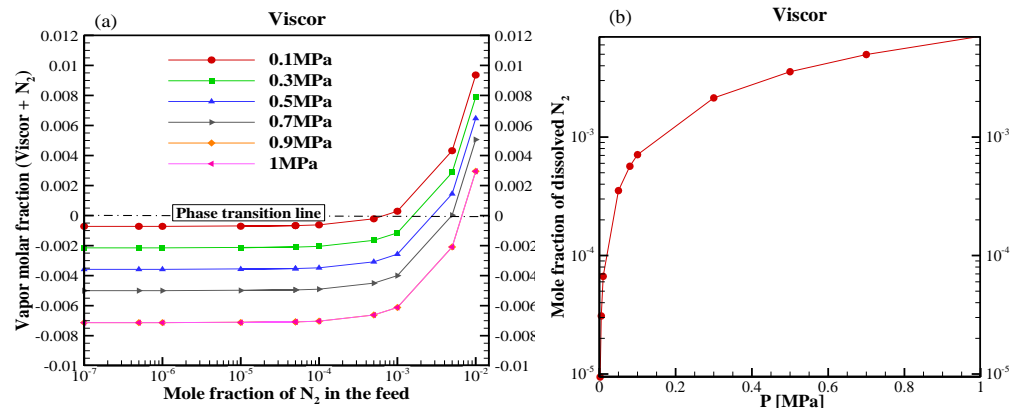
15

### 3. 3D cavitating nozzle simulation

16 Firstly, a thermodynamics study of the effect of non-condensable gas ( $N_2$ ) on the  
 17 phase change behaviour is conducted. Then the simulation results of a 3D cavitating  
 18 nozzle along with a detailed analysis of cavitation inception, nucleation and  
 19 turbulence are reported. The fuel used for cavitation modelling in this study is gasoline  
 20 calibrated fluid (Viscor 16BR) referring to the relevant experiments [15], [42]. Since  
 21 the real fluid EoS is employed, the involved input parameters like critical points and  
 22 acentric factor have referred to the properties of n-decane.

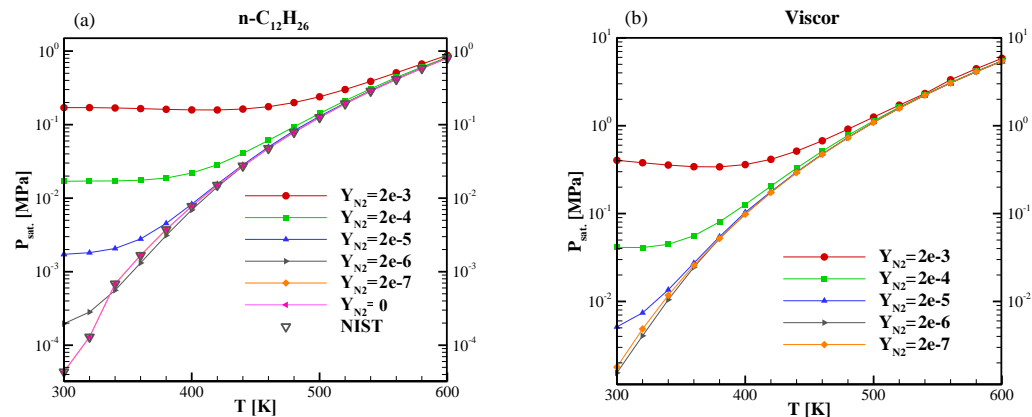
### 3.1 Thermodynamics study of the effect of non-condensable gas on phase change

To investigate the thermodynamic equilibrium behaviour of Viscor and  $N_2$  system, the method that is generally utilized at given temperature and pressure is the isothermal flash computation (TP flash) as noted in STEP 3 (Table 1). An important variable to represent the generated vapor at phase equilibrium calculation is the vapor mole fraction, ( $\psi_v$ ). This parameter indicates the overall amount of vapor which includes the vaporized fuel and the gaseous  $N_2$  that was dissolved in the liquid phase. Figure 4 (a) illustrates the evolution of  $\psi_v$  with the amount of  $N_2$  within the pressure range of 1 bar to 10 bar. As shown in Figure 4, one may see that the total vapor amount  $\psi_v$  has increased with the addition of  $N_2$  in the feed. This implies the compressed fuel initially containing a high amount of  $N_2$  will promote cavitation inception (or homogeneous nucleation). Some researcher has validated this phenomenon with experiments [64], in which they have attributed the intensifying of cavitation to the increase of cavitating nuclei coming from the dissolved gas. The dissolved gas can help decrease the energy needed to form a bubble and reduce the tensile strength of the fluid. One noting point in Figure 4 is that at each pressure, there exists a transition point where the  $\psi_v$  is changing from a negative value to the positive one which actually denotes the gas has transformed (or transitioned) from the dissolved state to the free gas in the bubble. To some extent, this may indicate the initial formation of a nuclei. The negative vapor fraction implies no vapor is generated in the flow and the amount of nitrogen is actually fully dissolved inside the liquid phase. In other words, the fluid is in single liquid phase until a certain mole fraction of  $N_2$  is reached according to the pressure and temperature conditions. Meanwhile, the phase state has been through the transition from pure liquid to two-phase. In addition, with higher pressure, the  $N_2$  concentration needed for phase transition (or nucleation) also increases notably which proves that high pressure can dissolve more  $N_2$ . The exponential growth trend of molar fraction in the liquid phase (dissolved  $N_2$ ) with pressure is shown in Figure 4 (b).



1 Figure 4 (a) The variation of vapor mole fraction with the molar fraction of  $N_2$  at  $T = 293$  K;  $P = 1$ -10 bar. (b) The  
 2 evolution of dissolved amount of  $N_2$  with the pressure increasing from 0.01 bar to 10 bar.

3  
 4 It is well-known that cavitation incepts as the pressure drops to the saturation value.  
 5 Thus, saturation pressure is an important index to indicate the inception of cavitation.  
 6 The evolutions of saturation pressure with temperature for n-dodecane ( $n-C_{12}H_{26}$ ) and  
 7 Viscor fuels at different  $N_2$  concentrations are illustrated in Figure 5. The saturation  
 8 pressure of pure n- $C_{12}H_{26}$  computed with PR EoS has been compared to the reference  
 9 data from NIST [65] (Figure 5 (a)). As observed in this Figure, an excellent agreement  
 10 has been achieved at the temperature range of 300 K-600 K for pure n- $C_{12}H_{26}$ . In  
 11 addition, the saturated pressure of the mixture system is approaching the pure  
 12 component value as the  $N_2$  mass fraction ( $Y_{N_2}$ ) is less than  $2E-6$ . However, obvious  
 13 deviations are detected as  $Y_{N_2}$  is increased to  $2E-6$ . These deviations are more evident  
 14 at low temperature ( $\sim 300$  K) conditions. A significant increase of saturation pressure  
 15 is witnessed as  $Y_{N_2}$  climbs from  $2E-6$  to  $2E-3$ . A similar trend is also detected for the  
 16 Viscor fuel (Figure 5 (b)). Minor differences are found for the saturation pressure as  
 17 the  $N_2$  concentration is between  $2E-6$  and  $2E-7$  for Viscor. Since larger saturation  
 18 pressure corresponds to higher  $N_2$  concentration, this will facilitate the inception of  
 19 cavitation as confirmed in the following 3D simulation.  
 20



21 Figure 5 (a, b) illustrate the variation of saturation pressure for n-dodecane and Viscor systems at a temperature  
 22 range of 300 K-600 K with different  $N_2$  concentrations.  $Y_{N_2}$  denotes the mass fraction of  $N_2$ .

### 23 3.2 Simulation setup

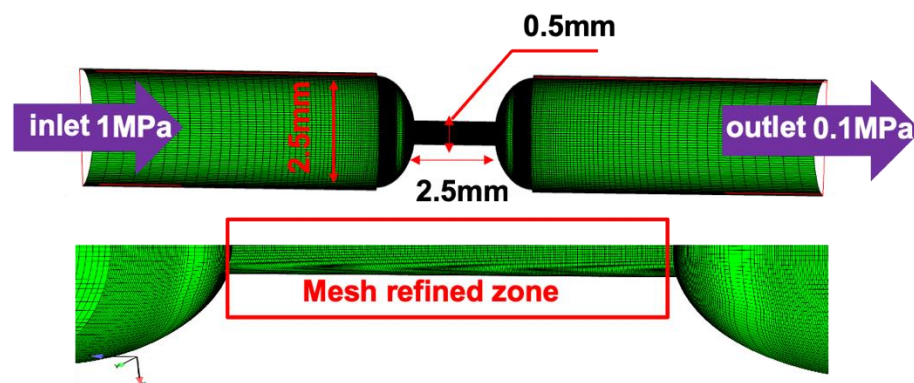
24 In this section, the fully compressible two-phase flow model based on phase  
 25 equilibrium theory is applied to simulate the cavitation phenomenon in a 3D real size  
 26 nozzle. The working fuel is gasoline calibrated fuel (Viscor 16BR) as noted above.  
 27 The involved non-condensable gas is  $N_2$ . The simulation results are compared to  
 28 available experimental data based on X-ray phase contrast imaging [66] and X-ray  
 29 radiography measurement [15]. The detailed numerical parameters are summarized  
 30 in Table 2.

This is the author's peer reviewed, accepted manuscript. However, the online version of record will be different from this version once it has been copyedited and typeset.  
PLEASE CITE THIS ARTICLE AS DOI:10.1063/1.5140981

1  
2  
3  
4  
5  
6  
7  
8  
9  
10

Table 2 Numerical parameters for the cavitation simulations

Simulation models	Fully compressible two-phase flow model
Cavitation model	Real fluid multi-component phase equilibrium solver
Initial N <sub>2</sub> mass fraction	Non-degas: 2E-5; Degas: 2E-6
Turbulence model	Large Eddy Simulation with Smagorinsky subgrid scale model
Grid type	Hexahedral
Minimum mesh resolution	5 $\mu\text{m}$
Time integration	First order
Spatial discretization	Secondary order
Boundary Conditions	Pressure inlet, $P_{\text{inlet}}$ : 1 MPa; Temperature $T_{\text{inlet}}$ : 293 K; $Y_{n_2, \text{inlet}}$ : 2E-5, 2E-6; Pressure outlet, $P_{\text{outlet}}$ : 0.1 MPa
Time step	2E-10 - 4E-10, CFL: 0.2
Initial nozzle condition	Submerge state, $T$ : 293 K, $P$ : 0.1 MPa, $V$ : 0 m/s



11 Figure 6 Configuration of 1/2 geometry and mesh refining zone with a total of 560425 cells and the minimum  
12 grid resolution is 5  $\mu\text{m}$ . The diameter of the orifice is 0.5 mm and its length is 2.5 mm [15]. The fluid flows from  
13 the left inlet to the right outlet with the pressure gradient of 1MPa to 0.1 MPa.  
14



1 The configuration of the nozzle is illustrated in Figure 6. The diameter of the orifice is  
2 500  $\mu\text{m}$ . Detailed descriptions can be found in Ref. [15]. Due to the limited  
3 computational resource, only half of the geometry is simulated. There are around 64  
4 cells across the orifice diameter which corresponds to an average cell size of 7.84  $\mu\text{m}$ .  
5 The refined mesh zones are distributed inside the orifice, the inlet and outlet regions,  
6 as shown in Figure 6.

7 Since the original experiments are performed in the submerged conditions [42][15],  
8 the simulation also assumes the initial conditions in the nozzle to be full of liquid with  
9 a trifle amount of  $\text{N}_2$ , as summarized in Table 2. The inlet and outlet are set with  
10 pressure boundary conditions with the 10 bar and 1 bar, respectively, close to the  
11 experimental conditions [42][15].

12 Besides, as discussed in the Introduction, in the original experiments, the tested  
13 conditions have contained the degassed and non-degassed conditions. Since no exact  
14 quantified amount of  $\text{N}_2$  is identified in the fluid during experiments, it is essential to  
15 determine a critical value to differentiate the non-degassed situation from the  
16 degassed state, for the convenience of modelling. As shown in Figure 4(a), the fluid  
17 state has transformed from single liquid state to two-phase saturation state with the  
18 increase of  $\text{N}_2$  in the fluid mixture. As the fluid is still in pure liquid state,  $\text{N}_2$  is therefore  
19 fully dissolved in the fluid, and the trifle  $\text{N}_2$  amount is exactly the same as the amount  
20 of dissolved  $\text{N}_2$ . Two initial values for the mass fraction of  $\text{N}_2$ ,  $Y_{\text{N}_2}$  equalling to (2E-5,  
21 2e-6) are selected to represent the non-degassed and degassed state, respectively.  
22 The amount of  $\text{N}_2$  in the non-degassed state is the same as the work of Battistoni [20].  
23 In contrast, the  $\text{N}_2$  concentration in the degassed state setting with 2E-6 is slightly  
24 higher than previous work (2E-7 in [20]) because in the current study,  $\text{N}_2$  is in the  
25 dissolved state unlike in [20] conditions where  $\text{N}_2$  is instead in the free gas state.

26 All the cavitation simulations are conducted with a finite volume scheme within the  
27 large eddy simulation framework. The involved sub-grid scale (SGS) model for the  
28 turbulence is the Smagorinsky model.

### 29 **3.3 Model assessment against X-ray Radiography data**

30 The original experiments [42][15] have been conducted under the non-degassed and  
31 degassed conditions with the nozzle made of different materials (plastic, metal).  
32 Obvious differences are found for the results obtained with these different materials.  
33 As discussed in the Introduction, an extra void cloud is only detected with the plastic  
34 nozzle under the non-degassed situation [42](Figure 1). The effect of dissolved  $\text{N}_2$  is  
35 proven to be extremely weak when the metal nozzle is used [15](Figure 2). According  
36 to Duke et al. [42][15], the extra void zone is formed because of local imperfections  
37 (or roughness) on the plastic nozzle surface.

38 For the simulated cases  $Y_{\text{N}_2} = (2\text{E}-5, 2\text{E}-6)$ , the following analysis is based on a limited  
39 computational time: 0.36 ms and 0.44 ms, respectively. Although both cases have not  
40 reached the quasi-steady flow, the following comparisons with the experiments based

1 on the latest time instants have proved to be appropriate, particularly near the hole  
2 entrance and the orifice wall where the cavitation is the most intense. Therefore, the  
3 following discussions will focus on the model assessment against X-ray phase contrast  
4 imaging and X-ray Radiography data. However, because of the nozzle made of  
5 different materials (plastic, metal) and also the fact that initial  $Y_{N2}$  is unknown in the  
6 experiments, the comparison of the numerical results with experiments can only be  
7 qualitative.

8 It is also noteworthy that considering the compressibility of the liquid and gas mixtures,  
9 our model has improved the speed accuracy of traveling waves in the computational  
10 domain between the inlet and outlet, but these waves have led to longer CPU time to  
11 reach steady state compared to previous studies [20].

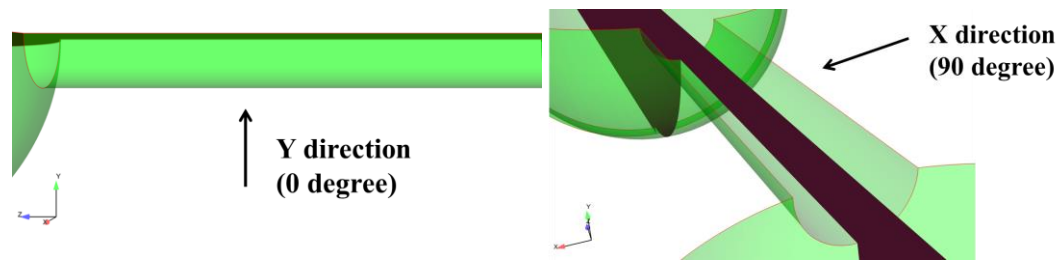
12 The numerical results are calculated based on the integrated void fraction ( $\alpha_g$ ) along  
13 the cast ray for both cases, the same as in the X-ray experiments. The line of sight  
14 integrations are performed in the  $Y(0^\circ)$  direction as well as the rotated  $X(90^\circ)$   
15 direction, as illustrated in Figure 7. One noting point is that the experimental images  
16 relating to the X-ray integrated void fraction are the time-averaged results collected  
17 at the steady flow state. Therefore, it is not appropriate to compare the instantaneous  
18 LES contour to the averaged experimental images shown in Figure 1 and Figure 2.  
19 Instead, the instantaneous X-ray phase contrast images from the experiments [42],  
20 [66] are displayed to compare with the simulated contour, as shown in Figure 8 and  
21 Figure 9, respectively. It is evident to observe from Figure 9 that the model can  
22 accurately capture the main cavities in the entrance and along the wall for both cases.  
23 In the experiments, because of the effect of defects in the plastic nozzle surface, more  
24 cavities are detected for the case with dissolved gas as marked in the circle in Figure  
25 8 [66]. It seems that the dissolved gas adhering to the surface of defects has  
26 functioned as nuclei for the extra cavitating zones.

27 As for the numerical results, the cavitation structure and behaviours have proved to  
28 be very different in the degassed and non-degassed cases. First, the cavitation in the  
29 degassed case is much more intense than in the non-degassed case. In addition, it is  
30 more fragmented and dispersed for the degassed case which may be attributed to  
31 stronger waves unsteadiness and turbulence as shown in the following discussions.  
32 However, such dispersed cavitation is not detected in the experimental results. But  
33 surprisingly, the steady cavitation structure in the experimental degassed case has  
34 presented some resemblance with the numerical non-degassed case. Therefore, the  
35 real amount of non-condensable gas in the experiments is probably far exceeding the  
36 adopted values (2E-5 and 2E-6) in this work. Yet, the obtained numerical results for  
37 the non-degassed case has proved to be quantitatively close to the X-ray experimental  
38 data, as discussed below.

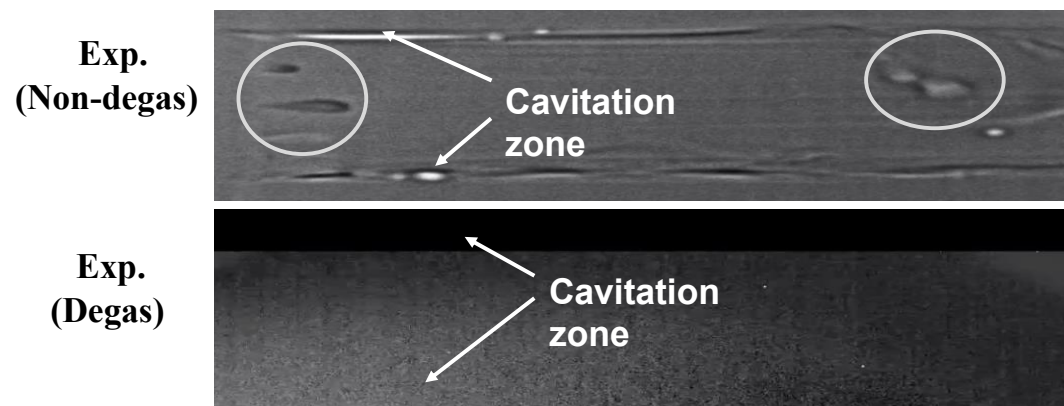
39 Since only half geometry is simulated in this work, the radiography results for the  
40 other half nozzle have been obviously assumed the same as the simulated half-nozzle.

41 Thus, the numerical radiography results shown in Figure 9 in the  $Y(0^\circ)$  direction are

1 computed (then doubled) accordingly. On the other hand, the radiography contour  
 2 for the non-simulated half-nozzle in the  $X$  ( $90^\circ$ ) direction is also taken as the  
 3 symmetry of the simulated results in Figure 9. Besides, in the  $X(90^\circ)$  direction, the line  
 4 of sight integration path covers the whole nozzle. Therefore, in this case, the  
 5 numerical radiography results depicted in Figure 9 are post-processed in a more  
 6 straightforward manner. As shown in Figure 9, the inlet sharp corner cavitation can be  
 7 captured correctly with current LES simulations. Whereas, affected by unsteadiness  
 8 and turbulence, the cavitation is not evenly distributed in the  $0^\circ$  and  $90^\circ$  directions,  
 9 for both  $N_2$  concentration cases. With limited computational time, the void  
 10 distribution seems not fully extended to the exit of the orifice for the non-degassed  
 11 case. However, the cavitating flow is very close to the steady state.  
 12



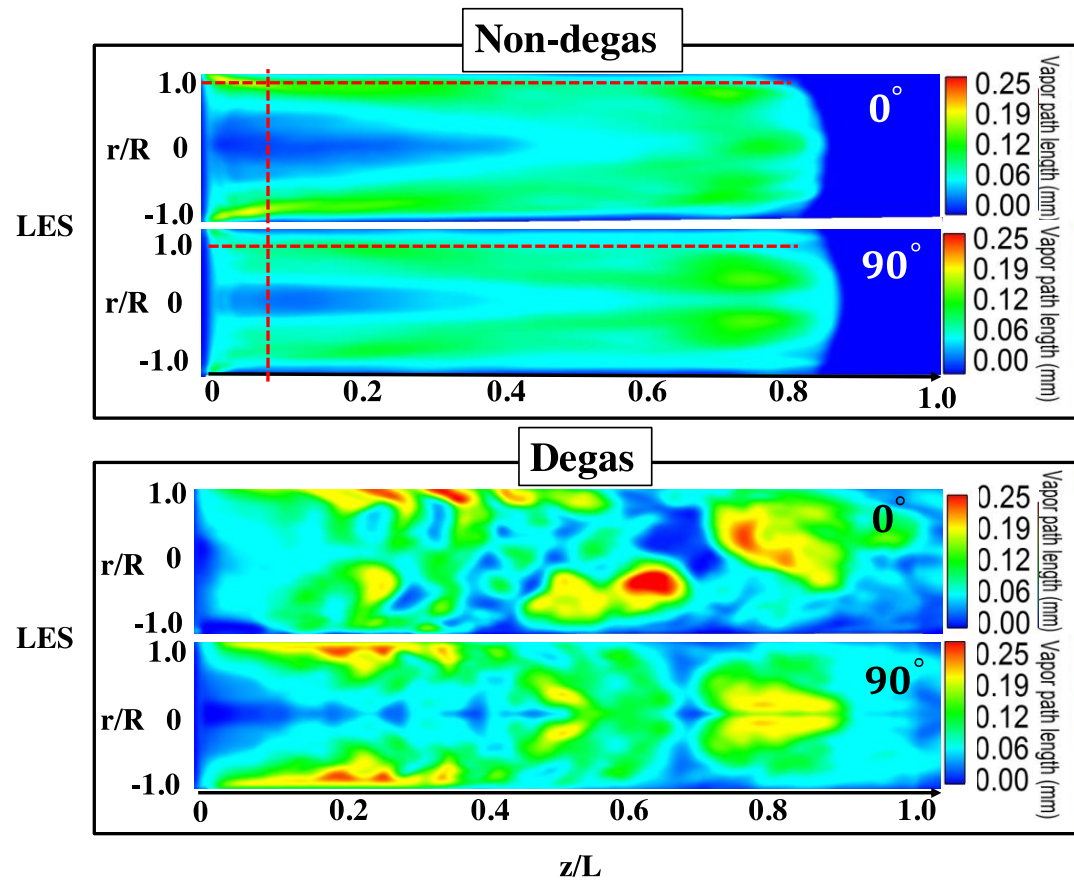
13  
 14  
 15 **Figure 7** Demonstration of numerical radiography projection direction.  $X$  direction denotes the rotated view  
 16 based on the  $Y$  direction.  
 17



18  
 19 **Figure 8** Instantaneous X-ray phase contrast images relating the cavitating nozzle performed with the non-  
 20 degassed fuel and degassed fuel. The experimental images are snapped directly from the video in the website  
 21 [67] with permission of Argonne National Laboratory. The wall cavitation is in the bright zones as illustrated by  
 22 the arrows. The cavities marked in the circles are induced by the defects of the nozzle. The flow is from left to  
 23 right.  
 24  
 25

This is the author's peer reviewed, accepted manuscript. However, the online version of record will be different from this version once it has been copyedited and typeset.

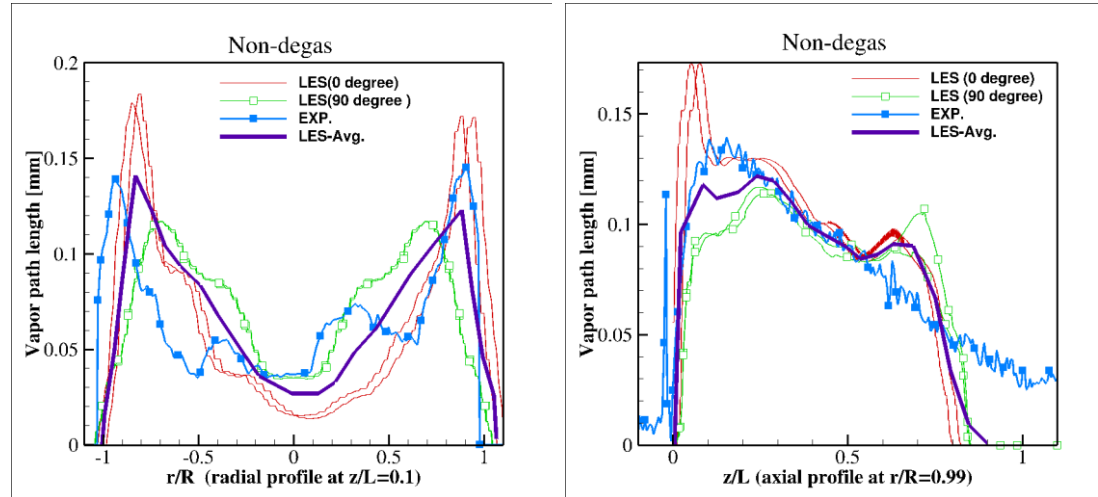
PLEASE CITE THIS ARTICLE AS DOI:10.1063/1.5140981



1  
2 **Figure 9** Contour plots of the numerical radiography based on the line of sight integration of volume fraction of  
3 gas ( $\alpha_g$ ) for the non-degassed case ( $Y_{N_2} = 2E - 5$ ,  $t = 0.36$  ms) and degassed case ( $Y_{N_2} = 2E - 6$ ,  $t = 0.44$  ms).  
4 The  $0^\circ$  view and  $90^\circ$  view denote the radiography are along  $X$  and  $Y$  direction, respectively. The fluid is from  
5 left to right.

6  
7 As aforementioned, since the numerical results of the non-degassed case show high  
8 resemblance to the experimental results qualitatively, a further quantitative  
9 comparison with the latest experimental results is conducted to assess the numerical  
10 model. Two profiles of void fraction have been plotted in the locations near the hole  
11 entrance and close to the orifice wall (see dashed lines in Figure 9) where the  
12 cavitation is most intense. More precisely, the radial profiles are at the axial distance  
13 of  $z/L = 0.1$  ( $z$  is the axial distance from hole inlet and  $L$  is the length of the hole) and  
14 the axial profiles are plotted along the wall of the orifice at ( $r/R = 0.99$ ) ( $r$  is the radial  
15 distance and  $R$  is the hole radius). To ensure the accuracy of the averaged results,  
16 several numerical results are collected around the targeted position within a deviation  
17 of 0.05 mm. As it may be observed in Figure 10, the numerical axial and radial profile  
18 shapes follows the experimental results well, but these are somewhat overestimated  
19 in the near wall for the  $0^\circ$  direction integration and underestimated for the  $90^\circ$   
20 direction. Therefore, the averaged value of the two directions corresponds better to

1 the averaged experimental profiles, as depicted in Figure 10. The uneven distribution  
 2 of the void fraction as aforementioned can be observed both in axial and radial  
 3 directions. It is undeniable that averaging the LES results based on longer  
 4 computational time as well as realizing the spatial averaging (through computing the  
 5 entire geometry) would better highlight the correspondence with the averaged  
 6 experimental results. This will be confirmed in future work.  
 7



8 **Figure 10** Quantitatively comparison between the averaged radiography experimental data [15] and the LES results  
 9 for the non-degassed case ( $Y_{N_2} = 2E - 5$ ,  $t = 0.36$  ms).

10

### 11 3.4 Effect of $N_2$ on cavitation inception

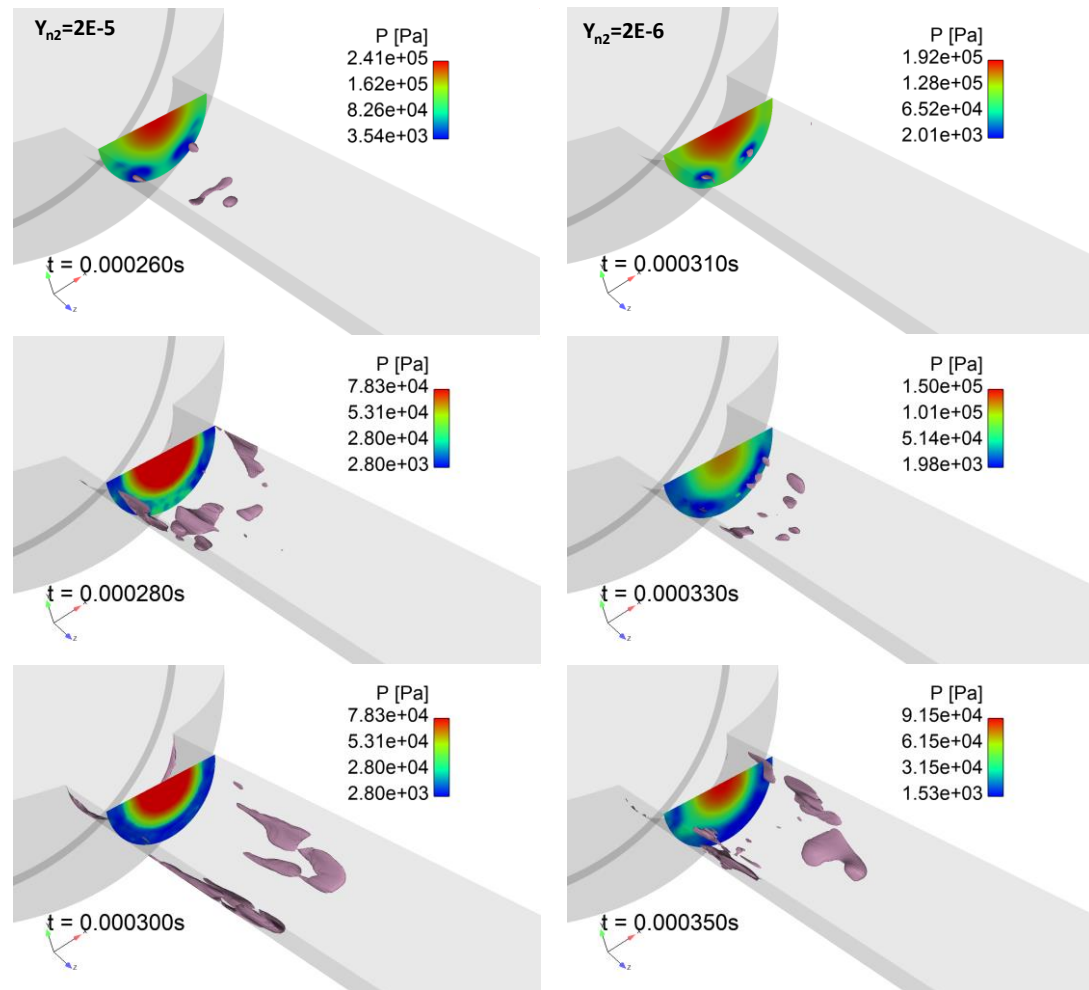
12 As discussed in the previous Section 3.1, higher  $N_2$  concentration in the fluid will bring  
 13 about the elevation of vapor pressure and the reduction of tensile strength for the  
 14 cavitation inception. Therefore, one may expect that the cavitation will incept earlier  
 15 in the case with more  $N_2$ . Indeed, as displayed in Figure 11, where the cavitation zone  
 16 is shown with the iso-surface ( $\alpha_g = 0.5$ ), the cavitation in the case with higher amount  
 17 of  $N_2$  ( $Y_{N_2} = 2E - 5$ ) starts at earlier time, around  $260 \mu s$ , than in the case with less  
 18  $N_2$  ( $Y_{N_2} = 2E - 6$ ) for which the inception of cavitation is severely lagged up to  
 19 around  $310 \mu s$ .

20 The minimum pressure is also larger for the fluid with more  $N_2$  at the location of  
 21 cavitation inception, as shown in the palette of Figure 11. Hence this result is  
 22 consistent with the fact that vapor pressure increases with higher amount of nitrogen,  
 23 as discussed previously in Section 3.1. One noting point is that the cavitation has not  
 24 appeared in the inlet corner of the orifice for both cases. Instead, it starts in the shear  
 25 stress layer as shown in the velocity contour in Figure 12. This phenomenon has been  
 26 confirmed in recent experimental observation [68]. As a matter of fact, the cavitation

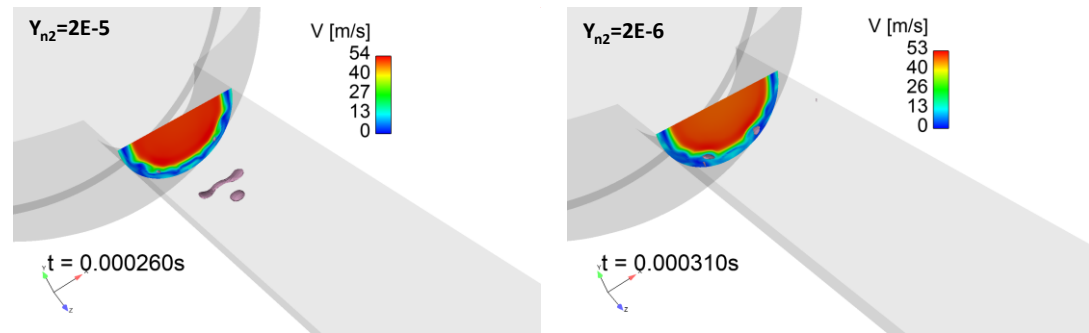
27 has incepted at the position of  $Z/L = 0.1$  where the pressure clip-planes are depicted  
 28 in Figure 11. Then, the formed nuclei are transported downstream with the flow.

This is the author's peer reviewed, accepted manuscript. However, the online version of record will be different from this version once it has been copyedited and typeset.  
PLEASE CITE THIS ARTICLE AS DOI:10.1063/1.5140981

1 Meanwhile, more regions start cavitating. It is interesting to detect that with similar  
2 time interval ( $20 \mu\text{s}$ ) in Figure 11, the cavity formation and growth rate is much larger  
3 for the flow with higher amount of  $\text{N}_2$ , as observed at the time interval [ $260 \mu\text{s}$ ,  $280 \mu\text{s}$ ],  
4 compared to the time interval [ $310 \mu\text{s}$ ,  $330 \mu\text{s}$ ]. This implies that the dissolved gas  
5 promotes the growth rate of the bubbles in addition to facilitating the inception of  
6 bubbles nuclei. With more non-condensable gas in the fluid, the maximum velocity  
7 proved to be slightly higher ( $54 \text{ m/s}$  instead of  $53 \text{ m/s}$ ) as shown in the velocity contour  
8 (Figure 12).  
9



10  
11 **Figure 11 Demonstration of the effect of  $\text{N}_2$  on cavitation inception and developing processes. The cavity is**  
12 **presented with the iso-surface of gas volume fraction ( $\alpha_g = 0.5$ ). The left and right column of images corresponds**  
13 **to the Case  $Y_{N_2} = 2E-5$  and Case  $Y_{N_2} = 2E-6$ , respectively.**  
14

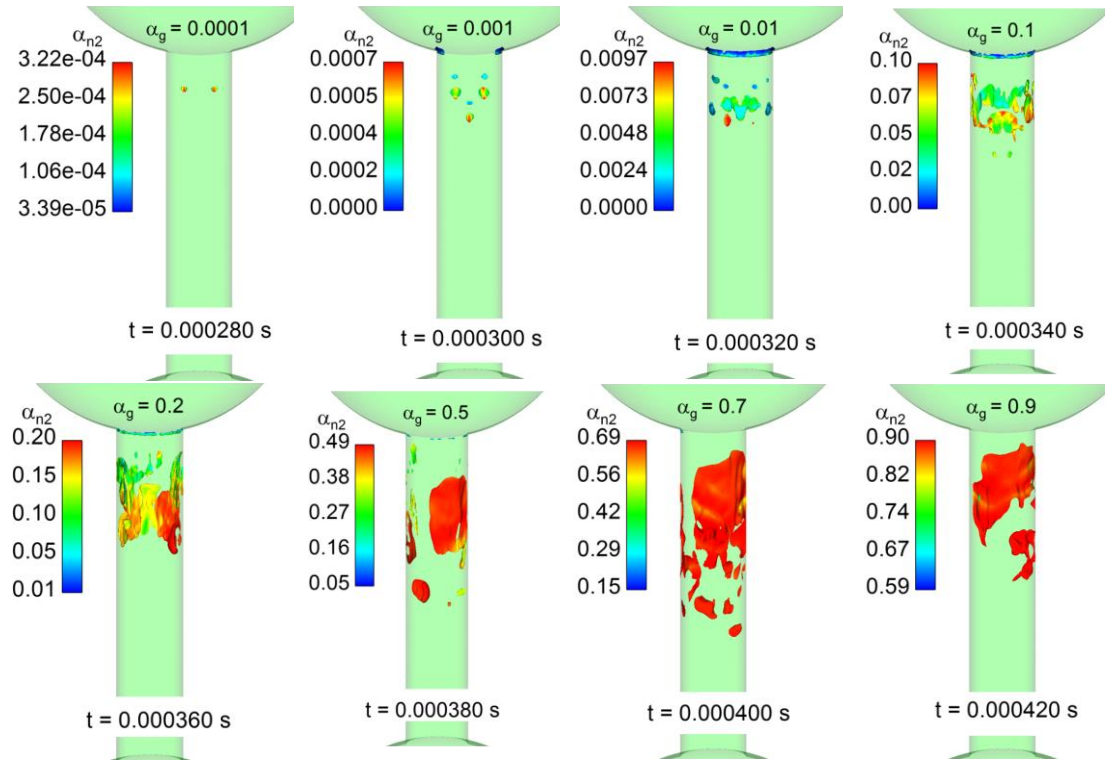


1 **Figure 12 Demonstration of the effect of  $N_2$  on the velocity contour at the location of cavitation inception.**  
 2 **The left, right column of images corresponds to the Case  $Y_{N_2} = 2E-5$  and Case  $Y_{N_2} = 2E-6$ , respectively.**

### 3 **3.5 Effect of $N_2$ on cavitation evolving**

4 With the phase equilibrium model developed in this work, the detailed analysis of the  
 5 homogeneous nucleation process becomes possible when the capillary effect is  
 6 neglected. Indeed, the current test cases have demonstrated the process of phase  
 7 transition from a multicomponent (Viscor,  $N_2$ ) single-phase flow to a two-phase flow  
 8 inside the orifice, automatically. In this section, phase transition (i.e. nucleation) is  
 9 discussed further, as it constitutes one of the most important novelties of this work.  
 10 The following discussion is based on the degassed case ( $Y_{N_2} = 2E-6$ ). In this case, it is  
 11 proved that the initial fluid is thermodynamically in single-phase. The phase transition  
 12 (i.e. nucleation) from a single phase (multicomponent liquid) towards a two-phase,  
 13 then further to a single phase gas state, corresponds to the formation of resolved  
 14 bubbles, as shown in Figure 13. For instance, the phase transition phenomenon may  
 15 be observed in this figure while the gas volume fraction ( $\alpha_g$ ) is increasing  
 16 progressively up to  $1 E-2$  during the period (280-320)  $\mu s$ . The initial nuclei keep  
 17 growing from the fully dissolved  $N_2$  state ( $\alpha_g < 1E - 4$ ) to a two-phase situation, and  
 18 finally to free gas ( $\alpha_g \geq 0.99$ ) with enough long time, as shown in Figure 13. One  
 19 noting point is the evolution of the volume fraction of the  $N_2$  in the gas cavities ( $\alpha_{g,N_2}$ )  
 20 which is defined with the formula  $\alpha_{g,N_2} = \alpha_g * y_{N_2}$ , where  $y_{N_2}$  is the molar fraction  
 21 of  $N_2$  in the gas phase. The  $N_2$  amount in the nuclei has kept increasing and almost 90%  
 22 of the cavities are filled with  $N_2$  as time evolves to 0.38 ms. However, in the earlier  
 23 period (280-360)  $\mu s$ , the amount of  $N_2$  is lower than half of the overall gas cavity  
 24 volume. In the phase equilibrium model, restricted by the constraint  $y_{N_2} + y_{viscor} =$   
 25 1 in gas phase, the evolving of the amount of the vaporous fuel and  $N_2$  are mutually  
 26 affected, which also implies that the gaseous cavitation and vaporous cavitation  
 27 processes are mutually impacted. According to the current numerical results,  
 28 vaporous cavitation is the dominant phase transition process during the nucleation  
 29 stage. Then, gaseous cavitation becomes more critical during the growth of the  
 30 cavities. It is therefore undeniable that gaseous cavitation plays a major role in the  
 31 later stage according to the current results. Another interesting point is that the  
 32 evolving process has seen the collapse of vaporous bubbles, especially at later stage

1 as shown in Figure 13 for  $t > 0.38$  ms. In addition, only gaseous (or non-condensable)  
 2 cavitation seems to survive in the later stage.  
 3  
 4



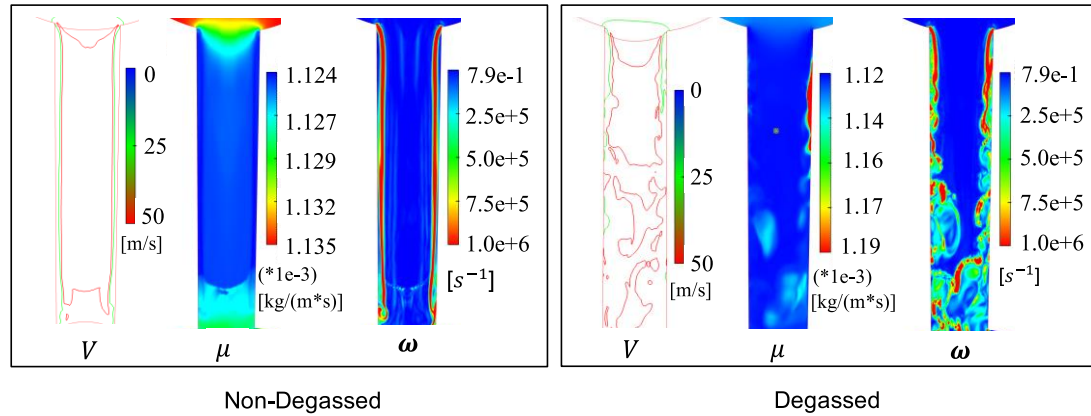
5  
 6 **Figure 13 Demonstration of nucleation and cavitating process within the time intervals of 0.14 ms. The cavitating**  
 7 **zone is presented by iso-surfaces of different void fraction ( $\alpha_g$ ) indicated at the top of each image. The iso-**  
 8 **surfaces are colored by the amount of gas  $N_2$  in the gas phase ( $\alpha_{n2} = \alpha_{g,N2}$ ), as shown by the different palettes.**  
 9

### 10 **3.6 Effect of $N_2$ on unsteadiness and turbulence**

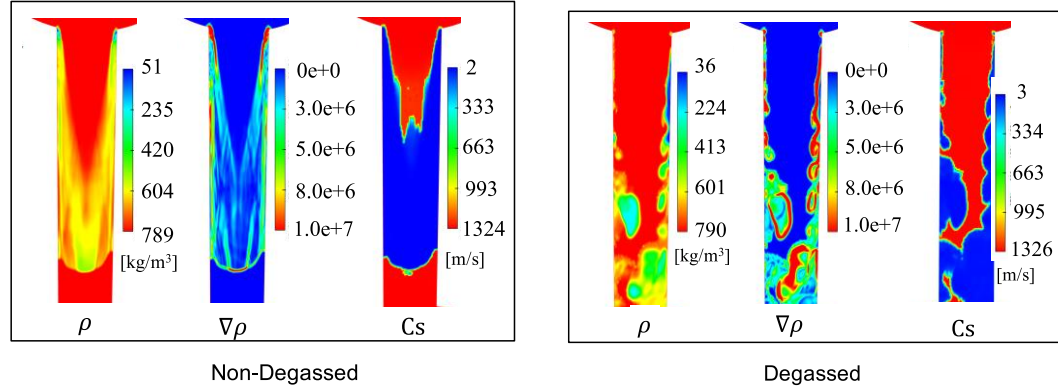
11 As aforementioned, the case with less non-condensable gas has shown stronger  
 12 unsteadiness and turbulence compared to the one with more non-condensable gas.  
 13 This is further clarified in the contour plots of velocity, eddy viscosity and vorticity, as  
 14 shown in Figure 14. The turbulent viscosity is much larger for the degassed case. More  
 15 complex vorticity is also detected in this case. The generation of vorticity is attributed  
 16 to more intense cavitation and collapse, as observed in previous PIV experimental  
 17 observations [69]. One could also observe the vorticity streaks generated especially at  
 18 the orifice entrance in the non-degassed case. Indeed, they are very similar to the  
 19 structures observed experimentally in Figure 8 also for the non-degassed case. In  
 20 addition, in contrast with the non-degassed case where the flow is relatively smooth,  
 21 the vorticity and the turbulent eddies are convected downstream but also towards  
 22 the hole axis, as could be noticed in Figure 14 in degassed case. More intense  
 23 cavitation is also witnessed for the degassed case which may be again verified by the



1 smaller density and larger density gradient (Figure 15). In this Figure, a large two-  
 2 phase region is formed especially in the second half of the nozzle for both non-  
 3 degassed and degassed cases, which corresponds to the regions with the smallest  
 4 sound speed. This is witnessing the local Mach number has far exceeded one, which  
 5 denotes the flow has entered the supersonic regime. This implies that it is important  
 6 to take into account the compressibility of the liquid for the cavitation simulation  
 7 which may explain why the stationary state is too long to reach.  
 8



9  
 10 **Figure 14** Contour plots of velocity ( $V$ ), eddy-viscosity ( $\mu$ ) and vorticity ( $\omega$ ) for the non-degassed and degassed  
 11 cases. The clip plane is the symmetry plane of the nozzle geometry normal to  $Y$  direction (see Figure 7).  
 12



13  
 14 **Figure 15** Contour plots of density ( $\rho$ ), density gradient ( $\nabla\rho$ ) and speed of sound ( $C_s$ ) for the non-degassed and  
 15 degassed cases. The clip plane is the symmetry plane of the nozzle geometry normal to  $Y$  direction (see Figure  
 16 7).  
 17  
 18  
 19  
 20  
 21  
 22  
 23

#### 1           **4. Conclusions and challenges**

2           A fully compressible two-phase flow model based on phase equilibrium theory with  
3           real fluid equation of state has been described in the current study. The capability of  
4           fluid transition from pure liquid to two-phase state has been firstly verified through  
5           stand-alone vapor-liquid equilibrium computation. It is shown that with the addition  
6           of  $N_2$ , the involved non-condensable gas can evolve from the dissolved state to free  
7           gas state. Besides, more  $N_2$  can be dissolved at high pressure. Then, the model was  
8           applied to simulate the cavitation phenomenon inside a single-hole nozzle to  
9           investigate the effect of dissolved  $N_2$  on the cavitation behaviour. The obtained quasi-  
10          steady results are quantitatively comparable to the X-ray experimental results. Several  
11          conclusions are summarized from the LES simulations:

12           1) With real-fluid phase equilibrium solver, the model is able to dynamically  
13           predict the phase transition process such as the nucleation phenomenon and  
14           subsequent cavitation.

15           2) With more dissolved  $N_2$ , the cavitation inception time is much earlier than for  
16           degassed fluid.

17           3) With the formation and collapse of the void cavities, more turbulent  
18           unsteadiness is highlighted for the case with less  $N_2$ .

19          The two-phase flow model combined with a real-fluid phase equilibrium solver has  
20          been shown to have more advantages in revealing the cavitation physics details than  
21          previously published cavitation models using barotropic or incompressible liquid  
22          assumptions, for instance. According to the current numerical results, the fraction of  
23          non-condensable  $N_2$  in the gaseous cavities have been quantified. It turns out that  
24          vaporous cavitation is the dominant phase transition process during the nucleation  
25          stage especially in the fluid with minimal  $N_2$ . Then, gaseous  $N_2$  cavitation becomes  
26          more significant during the growth of the cavities.

27          Finally, one should admit that there are still several challenges to be addressed for  
28          proper cavitation simulations. The first and most important issue is computational  
29          efficiency. We found that more than 70% of the CPU time is consumed in the  
30          thermodynamic equilibrium computation. A possible solution to address this issue is  
31          using tabulation method [70], [71]. Indeed, all the thermal properties including phase  
32          composition, speed of sound, internal energy...etc, from phase equilibrium calculation  
33          could be stored in a table prepared before the simulation starts. This can avoid the  
34          time-consuming thermodynamics computation. The other encountered issue is the  
35          convergence problem as approaching the phase boundary. It is found that tons of  
36          iterations are needed to reach the convergence criterion at phase boundaries. The  
37          main reason is ascribed to the huge gradient of phase properties at the phase

This is the author's peer reviewed, accepted manuscript. However, the online version of record will be different from this version once it has been copyedited and typeset.

PLEASE CITE THIS ARTICLE AS DOI:10.1063/1.5140981

1 boundary. Potential numerical instabilities caused by the oscillations in the phase  
2 boundary are also witnessed. It is recommended to adopt better algorithm to resolve  
3 this issue. The current work is expected to provide some references for the cavitation  
4 modelling using real-fluid EoS.

5  
6  
7

## 8 Acknowledgement

9 This project has received funding from the European Union Horizon 2020 Research  
10 and Innovation program. Grant Agreement No 675528 for the IPPAD project. The  
11 author would like to acknowledge Dr. Daniel Duke for providing the experimental data.

12

## 1 References

- 2 [1] P. Koukouvinis, M. Gavaises, J. Li, and L. Wang, "Large Eddy Simulation of Diesel injector  
3 including cavitation effects and correlation to erosion damage," *Fuel*, vol. 175, pp. 26–39,  
4 2016.
- 5 [2] G. Kähler, F. Bonelli, G. Gonnella, and A. Lamura, "Cavitation inception of a van der Waals  
6 fluid at a sack-wall obstacle," *Phys. Fluids*, vol. 27, no. 123307, 2015.
- 7 [3] (张皓晨); H. Z., (左志钢); Z. Z., K. A. Mørch, and Shuhong Liu (刘树红), "Thermodynamic  
8 effects on Venturi cavitation characteristics," *Phys. Fluids*, vol. 31, no. 9, 2019.
- 9 [4] P. Koukouvinis, C. Bruecker, and M. Gavaises, "Unveiling the physical mechanism behind pistol  
10 shrimp cavitation," *Sci. Rep.*, vol. 7, no. 13994, 2017.
- 11 [5] W. H. Nurick, "Orifice Cavitation and Its Effect on Spray Mixing," *J. Fluids Eng.*, vol. 98, pp.  
12 681–687, 1976.
- 13 [6] F. Payri, V. Bermúdez, R. Payri, and F. J. Salvador, "The influence of cavitation on the internal  
14 flow and the spray characteristics in diesel injection nozzles," *Fuel*, vol. 83, no. 4–5, pp. 419–  
15 431, 2004.
- 16 [7] M. Blessing, G. König, C. Krüger, U. Michels, and V. Schwarz, "Analysis of Flow and Cavitation  
17 Phenomena in Diesel Injection Nozzles and Its Effects on Spray and Mixture Formation," in  
18 *SAE Technical Paper Series*, 2010.
- 19 [8] C. Habchi, N. Dumont, and O. Simonin, "Multidimensional Simulation of Cavitating Flows in  
20 Diesel Injectors By a Homogeneous Mixture Modeling Approach," *At. Sprays*, vol. 18, no. 2,  
21 pp. 129–162, 2008.
- 22 [9] H. Yu, L. Goldsworthy, P. A. Brandner, and V. Garaniya, "Development of a compressible  
23 multiphase cavitation approach for diesel spray modelling," *Appl. Math. Model.*, vol. 45, pp.  
24 705–727, 2017.
- 25 [10] H. K. Suh and C. S. Lee, "Effect of cavitation in nozzle orifice on the diesel fuel atomization  
26 characteristics," *Int. J. Heat Fluid Flow*, vol. 29, no. 4, pp. 1001–1009, 2008.
- 27 [11] C. Badock, R. Wirth, A. Fath, and A. Leipertz, "Investigation of cavitation in real size diesel  
28 injection nozzles," *Int. J. Heat Fluid Flow*, vol. 20, no. 5, pp. 538–544, 1999.
- 29 [12] D. Bauer, H. Chaves, and C. Arcoumanis, "Measurements of void fraction distribution in  
30 cavitating pipe flow using x-ray CT," *Meas. Sci. Technol.*, vol. 23, no. 5, p. 55302, 2012.
- 31 [13] E. Giannadakis, M. Gavaises, and C. Arcoumanis, "Modelling of cavitation in diesel injector  
32 nozzles," *J. Fluid Mech.*, vol. 616, pp. 153–193, 2008.
- 33 [14] D. J. Duke *et al.*, "X-ray radiography measurements and numerical simulations of cavitation in  
34 a metal nozzle," in *ILASS Americas 28th Annual Conference on Liquid Atomization and Spray  
35 Systems*, 2016, no. May.
- 36 [15] D. J. Duke *et al.*, "X-ray radiography of cavitation in a beryllium alloy nozzle," *Int. J. Engine  
37 Res.*, vol. 18, no. 1–2, pp. 39–50., 2017.
- 38 [16] J. M. Desantes, F. J. Salvador, M. Carreres, and J. Martínez-López, "Large-eddy simulation  
39 analysis of the influence of the needle lift on the cavitation in diesel injector nozzles," *Proc.  
40 Inst. Mech. Eng. Part D J. Automob. Eng.*, vol. 229, no. 4, pp. 407–423, 2014.

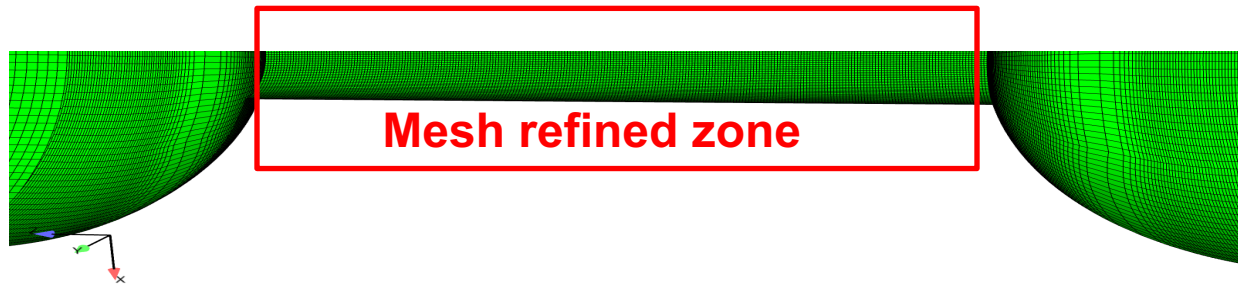
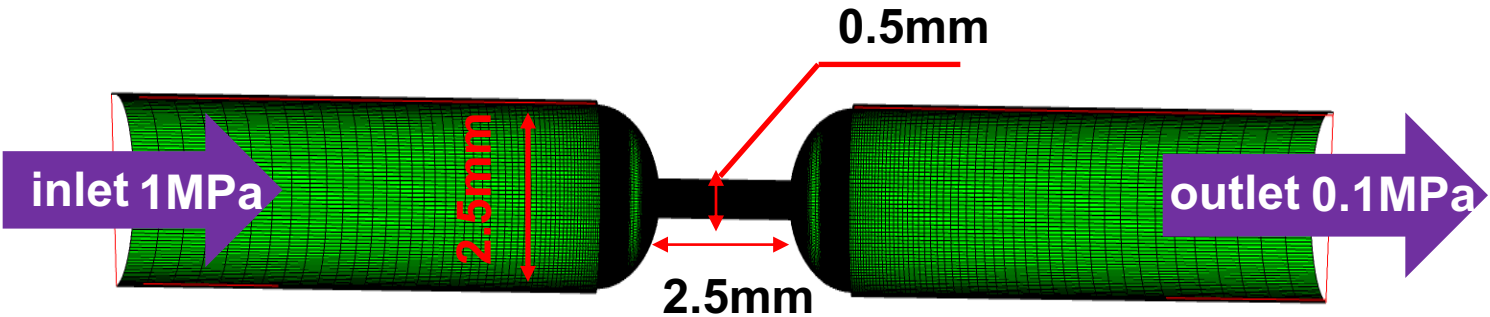
- 1 [17] S. Molina, F. J. Salvador, M. Carreres, and D. Jaramillo, "A computational investigation on the  
2 influence of the use of elliptical orifices on the inner nozzle flow and cavitation development  
3 in diesel injector nozzles," *Energy Convers. Manag.*, vol. 79, pp. 114–127, 2014.
- 4 [18] DELANNOY Y., "Two Phase Flow Approach in Unsteady Cavitation Modelling," in *Cavitation  
5 and Multiphase Flow Forum*, 1990.
- 6 [19] M. Battistoni, S. Som, and D. E. Longman, "Comparison of Mixture and Multifluid Models for  
7 In-Nozzle Cavitation Prediction," *J. Eng. Gas Turbines Power*, vol. 136, no. 6, p. 061506, 2014.
- 8 [20] M. Battistoni, D. J. Duke, A. B. Swantek, F. Z. Tilocco, C. F. Powell, and S. Som, "Effects of  
9 Noncondensable Gas on Cavitating Nozzles," *At. Sprays*, vol. 25, no. 6, pp. 453–483, 2015.
- 10 [21] C. Habchi, "a Gibbs Energy Relaxation (Germ) Model for Cavitation Simulation," *At. Sprays*,  
11 vol. 25, no. 4, pp. 317–334, 2015.
- 12 [22] Y. Wang, L. Qiu, R. D. Reitz, and R. Diwakar, "Simulating cavitating liquid jets using a  
13 compressible and equilibrium two-phase flow solver," *Int. J. Multiph. Flow*, vol. 63, pp. 52–67,  
14 2014.
- 15 [23] A. Alajbegovic, G. Meister, D. Greif, and B. Basara, "Three phase cavitating flows in high-  
16 pressure swirl injectors," *Exp. Therm. Fluid Sci.*, vol. 26, pp. 677–681, 2002.
- 17 [24] H. Roth *et al.*, "Effect of Multi-Injection Strategy on Cavitation Development in Diesel Injector  
18 Nozzle Holes," in *SAE Technical Paper Series*, 2005.
- 19 [25] X. Lyu, S. Pan, X. Hu, and N. A. Adams, "Numerical investigation of homogeneous cavitation  
20 nucleation in a microchannel," *Phys. Rev. FLUIDS*, vol. 064303, pp. 1–15, 2018.
- 21 [26] W. Yuan, J. Sauer, and G. H. Schnerr, "Modeling and computation of unsteady cavitation flows  
22 in injection nozzles," *Mec. Ind.*, vol. 2, no. 5, pp. 383–394, 2001.
- 23 [27] F. Petitpas, J. Massoni, R. Saurel, E. Lapebie, and L. Munier, "Diffuse interface model for high  
24 speed cavitating underwater systems," *Int. J. Multiph. Flow*, 2009.
- 25 [28] C. Rodriguez;, A. Vidal;, P. Koukouvinis;, M. Gavaises;, and M.A. McHug;, "Simulation of  
26 transcritical fluid jets using the PC-SAFT EoS," *J. Comput. Phys.*, vol. 374, pp. 444–468, 2018.
- 27 [29] J. Matheis and S. Hickel, "Multi-component vapor-liquid equilibrium model for LES of high-  
28 pressure fuel injection and application to ECN Spray A," *Int. J. Multiph. Flow*, no. October,  
29 2017.
- 30 [30] S. Yang, P. Yi, and C. Habchi, "Real-fluid injection modelling and LES simulation of the ECN  
31 Spray A injector using a fully compressible two-phase flow approach," *Int. J. Multiph. Flow*, p.  
32 103145, 2019.
- 33 [31] C. Habchi, J. Bohbot, A. Schmid, and K. Herrmann, "A comprehensive Two-Fluid Model for  
34 Cavitation and Primary Atomization Modelling of liquid jets - Application to a large marine  
35 Diesel injector," *J. Phys. Conf. Ser.*, vol. 656, no. 1, 2015.
- 36 [32] R. Saurel, P. Boivin, and O. Le Métayer, "A general formulation for cavitating, boiling and  
37 evaporating flows," *Comput. Fluids*, vol. 128, pp. 53–64, 2016.
- 38 [33] R. Saurel, F. Petitpas, and R. Abgrall, "Modeling phase transition in metastable liquids.  
39 pplication to flashing and cavitating flows," *Int. J. Multiph. Flow*, vol. 607, pp. 313–350, 2008.
- 40 [34] O. Le Métayer and R. Saurel, "The Noble-Abel Stiffened-Gas equation of state," *Phys. Fluids*,  
41 vol. 28, no. 4, pp. 0–33, 2016.
- 42 [35] L. M. Olivier, J. Massoni, and R. Saurel., "Élaboration des lois d'état d'un liquide et de sa

- 1           vapeur pour les modèles d'écoulements diphasiques," *Int. J. Therm. Sci.*, vol. 43, no. 3, pp.  
 2           265–276, 2004.
- 3   [36]   E. Lauer, X. Y. Hu, S. Hickel, and N. A. Adams, "Numerical modelling and investigation of  
 4           symmetric and asymmetric cavitation bubble dynamics," *Comput. Fluids*, vol. 69, pp. 1–19,  
 5           2012.
- 6   [37]   H. Yu, L. Goldsworthy, P. A. Brandner, J. Li, and V. Garaniya, "Modelling thermal effects in  
 7           cavitating high-pressure diesel sprays using an improved compressible multiphase approach,"  
 8           *Fuel*, vol. 222, pp. 125–145, 2018.
- 9   [38]   P. Yi, S. Yang, C. Habchi, and R. Lugo, "A multicomponent real-fluid fully compressible four-  
 10          equation model for two-phase flow with phase change," *Phys. Fluids*, vol. 31, no. 2, p. 026102,  
 11          2019.
- 12 [39]   R. Menikoff and B. J. Plohr, "The Riemann problem for fluid flow of real materials," *Rev. Mod.*  
 13          *Phys.*, 1989.
- 14 [40]   R. Saurel and P. Boivin, "Cavitation Instabilities and Rotordynamic Effects in Turbopumps and  
 15          Hydroturbines," vol. 575, no. January, 2017.
- 16 [41]   A. B. Wood., *A Textbook of Sound*. 1955.
- 17 [42]   D. J. Duke, A. L. Kastengren, F. Z. Tilocco, A. B. Swantek, and C. F. Powell, "X-Ray Radiography  
 18          Measurements of Cavitating Nozzle Flow," *At. Sprays*, vol. 23, no. 9, pp. 841–860, 2013.
- 19 [43]   D. J. Duke, A. L. Kastengren, A. B. Swantek, K. E. Matusik, and C. F. Powell, "X-ray fluorescence  
 20          measurements of dissolved gas and cavitation," *Exp. Fluids*, 2016.
- 21 [44]   M. Karaeen and E. Sher, "SPRAY CHARACTERISTICS OF DIESEL FUEL CONTAINING DISSOLVED  
 22          CO2 SPRAY CHARACTERISTICS OF DIESEL FUEL," *At. Sprays*, vol. 21, no. 11, 2011.
- 23 [45]   A. Rashkovan and E. Sher, "Flow pattern observations of gasoline dissolved CO2 inside an  
 24          injector," *At. Sprays*, vol. 16, no. 6, 2006.
- 25 [46]   I. Y. Senda J, Hashimoto K and F. H., "CO<sub>2</sub> Mixed Fuel Combustion System for Reduction of NO  
 26          and Soot Emission in Diesel Engine.," *SAE Trans.*, pp. 471–481, 1997.
- 27 [47]   A. Xiao, Jin, Zhen Huang, Ma Junjun and Q. Xinqi, "An experimental study on spray transient  
 28          characteristics in fuel containing CO<sub>2</sub>," *At. Sprays*, vol. 19, no. 4, 2009.
- 29 [48]   Z. Huang, Y. Shao, S. Shiga, and H. Nakamura, "Controlling mechanism and resulting spray  
 30          characteristics of injection of fuel containing dissolved gas," *J. Therm. Sci.*, vol. 3, no. 3, pp.  
 31          191–199, 1994.
- 32 [49]   H. Zhang, Z. Zuo, and S. Liu, "Influence of dissolved gas content on Venturi cavitation at  
 33          thermally sensitive conditions," in *Proceedings of the 10th International Symposium on*  
 34          *Cavitation (CAV2018)*, 2018, pp. 546–550.
- 35 [50]   A. Amini, M. Reclari, T. Sano, and M. Farhat, "Effect of Gas Content on Tip Vortex Cavitation,"  
 36          in *Proceedings of the 10th International Symposium on Cavitation*, 2018, pp. 322–325.
- 37 [51]   S. Gireesan and A. B. Pandit, "Modeling the effect of carbon-dioxide gas on cavitation,"  
 38          *Ultrason. - Sonochemistry*, vol. 34, pp. 721–728, 2017.
- 39 [52]   S. Yang, C. Habchi, P. Yi, and R. Lugo, "Cavitation Modelling Using Real-Fluid Equation of  
 40          State.," in *Proceedings of the 10th International Symposium on Cavitation(CAV2018)*, 2018.
- 41 [53]   S. Yang, "Modeling of Diesel injection in subcritical and supercritical conditions," University of  
 42          Paris-Saclay, 2019.

This is the author's peer reviewed, accepted manuscript. However, the online version of record will be different from this version once it has been copyedited and typeset.

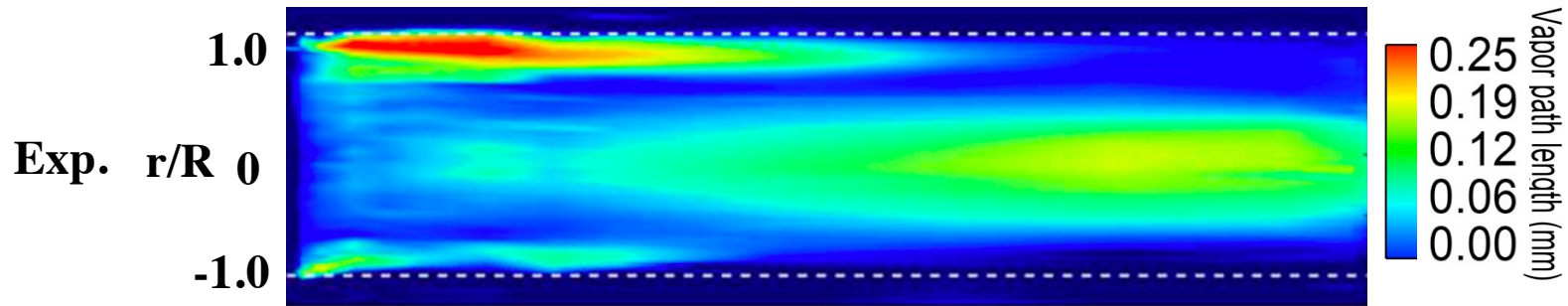
PLEASE CITE THIS ARTICLE AS DOI:10.1063/1.5140981

- 1 [54] M. S. Baer and J. W. Nunziato, "A two-phase mixture theory for the deflagration to detonation  
2 (DDT) transition in reactive granular materials," *Int. J. Multiph. Flow*, vol. 12, no. 6, pp. 861–  
3 889, 1986.
- 4 [55] T. C. Horng, M. Ajlan, L. L. Lee, K. E. Starling, and M. Ajlan, "Generalized Multiparameter  
5 Correlation for Nonpolar and Polar Fluid Transport Properties," *Ind. Eng. Chem. Res.*, vol. 27,  
6 no. 4, pp. 671–679, 1988.
- 7 [56] B. E. Poling, J. M. Prausnitz, and J. P. O'Connell, *The Properties of Gases and Liquids*. 2001.
- 8 [57] S. Saha and J. J. Carroll, "The isoenergetic-isochoric flash," *Fluid Phase Equilib.*, vol. 138, pp.  
9 23–41, 1997.
- 10 [58] F. A. Aly and L. L. Lee, "Self-consistent equations for calculating the ideal gas heat capacity,  
11 enthalpy, and entropy," *Fluid Phase Equilib.*, vol. 6, no. 3–4, pp. 169–179, 1981.
- 12 [59] G. Wilczek-Vera and J. H. Vera, "Understanding cubic equations of state: A search for the  
13 hidden clues of their success," *AIChE J.*, vol. 61, no. 9, pp. 2824–2831, 2015.
- 14 [60] J. Bohbot, N. Gillet, and A. Benkenida, "IFP-C3D: an Unstructured Parallel Solver for Reactive  
15 Compressible Gas Flow with Spray," *Oil Gas Sci. Technol.*, vol. 64(3), no. 3, pp. 309–335, 2009.
- 16 [61] S. Patankar, *Numerical heat transfer and fluid flow: Computational methods in mechanics and  
17 thermal science*. 1980.
- 18 [62] A. Zein, M. Hantke, and G. Warnecke, "Modeling phase transition for compressible two-phase  
19 flows applied to metastable liquids," *J. Comput. Phys.*, vol. 229, no. 8, pp. 2964–2998, 2010.
- 20 [63] A. Chiapolino, P. Boivin, and R. Saurel, "A simple and fast phase transition relaxation solver for  
21 compressible multicomponent two-phase flows," *Comput. Fluids*, vol. 150, pp. 31–45, 2017.
- 22 [64] B. Li, Y. Gu, and M. Chen, "An experimental study on the cavitation of water with dissolved  
23 gases," *Exp. Fluids*, vol. 58, no. 12, pp. 1–9, 2017.
- 24 [65] P. J. Linstrom and W. G. Mallard, "The NIST Chemistry WebBook: A chemical data resource on  
25 the Internet," *J. Chem. Eng. Data*, vol. 46, no. 5, pp. 1059–1063, 2001.
- 26 [66] D. Duke *et al.*, "X-ray Imaging of Cavitation in Diesel Injectors," *SAE Int. J. Engines*, vol. 7, no. 2,  
27 pp. 2014-01-1404, 2014.
- 28 [67] D. J. Duke, "<https://daniel-duke.net/media/> : Synchrotron X-ray Radiography of Nozzle  
29 Cavitation." .
- 30 [68] C. Mauger, L. Méès, M. Michard, A. Azouzi, and S. Valette, "Shadowgraph, Schlieren and  
31 interferometry in a 2D cavitating channel flow," *Exp. Fluids*, vol. 53, no. 6, pp. 1895–1913,  
32 2012.
- 33 [69] S. Gopalan and J. Katz, "Flow structure and modeling issues in the closure region of attached  
34 cavitation," *Phys. Fluids*, vol. 12, no. 4, 2000.
- 35 [70] P. Yi, S. Jafari, S. Yang, and C. Habchi, "Numerical analysis of subcritical evaporation and  
36 transcritical mixing of droplet using a tabulated multicomponent vapor-liquid equilibrium  
37 model," in *ILASS–Europe 2019, 29th Conference on Liquid Atomization and Spray Systems*,  
38 2019.
- 39 [71] S. Brown *et al.*, "Thermodynamic interpolation for the simulation of two-phase flow of non-  
40 ideal mixtures," *Comput. Chem. Eng.*, vol. 95, pp. 49–57, 2006.
- 41  
42

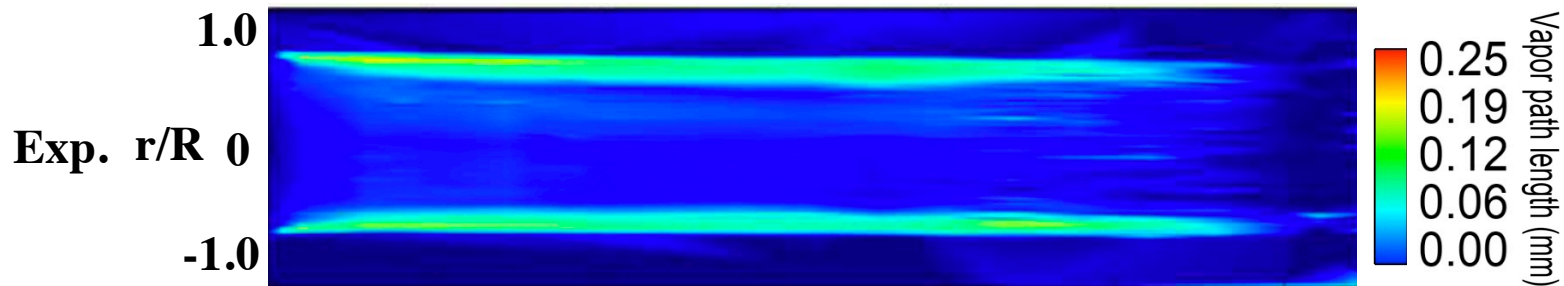




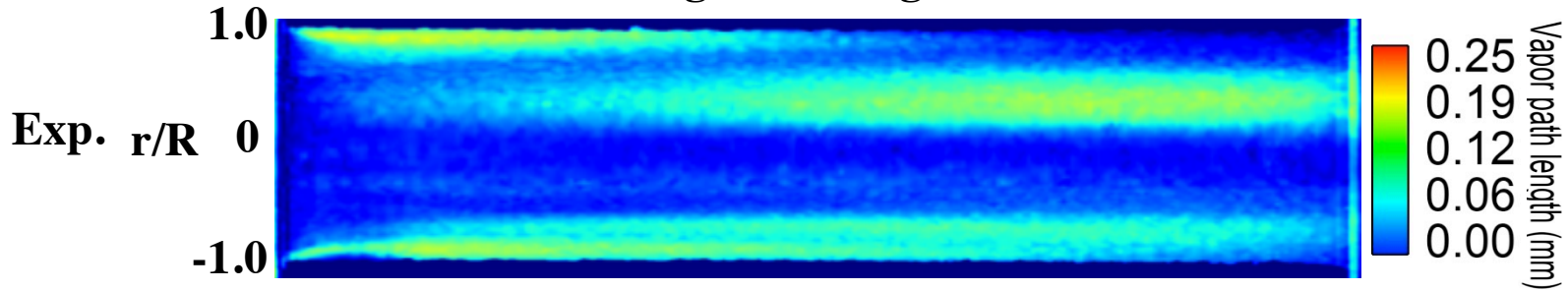
## Non-degassed fuel

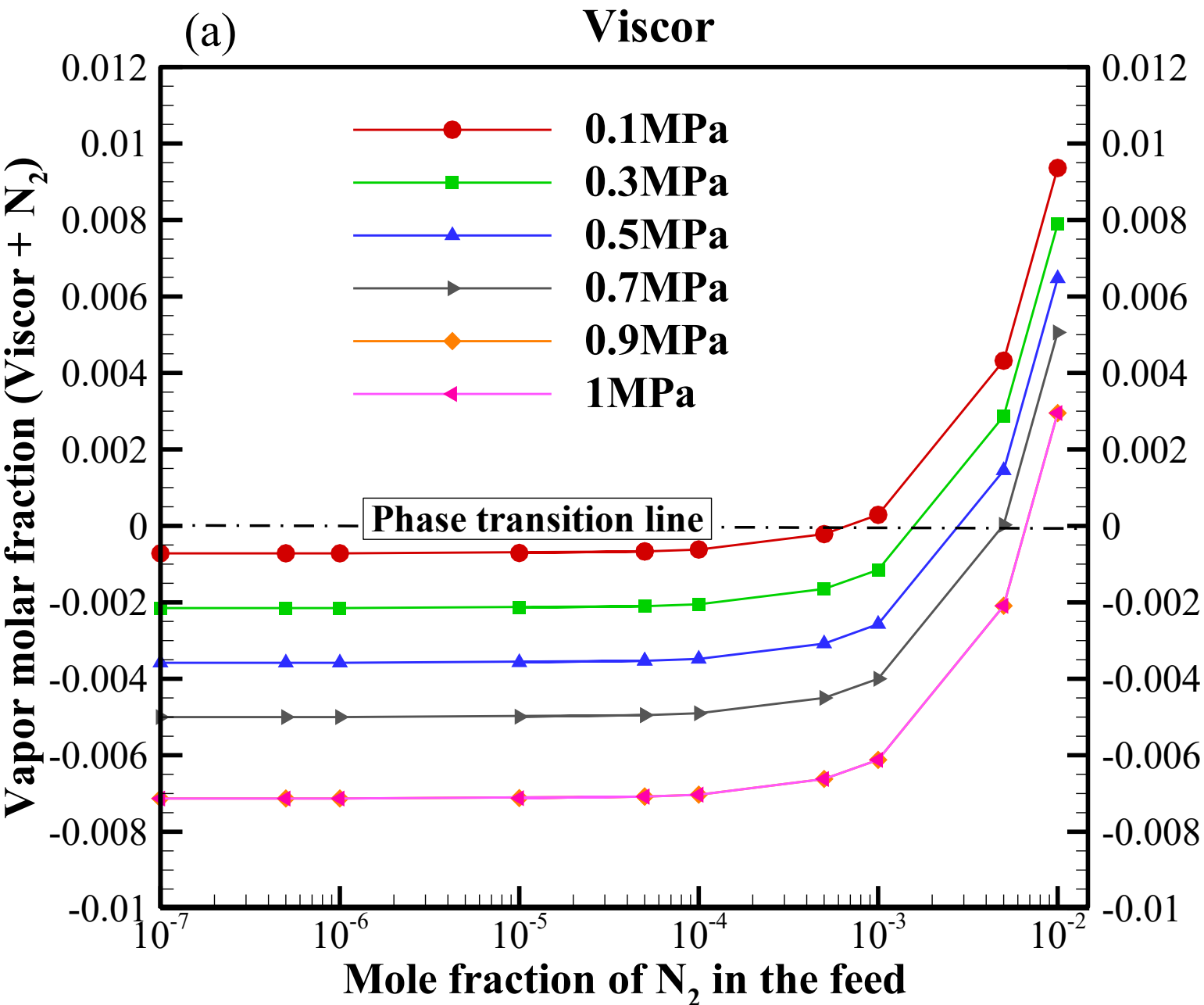


## Degassed fuel



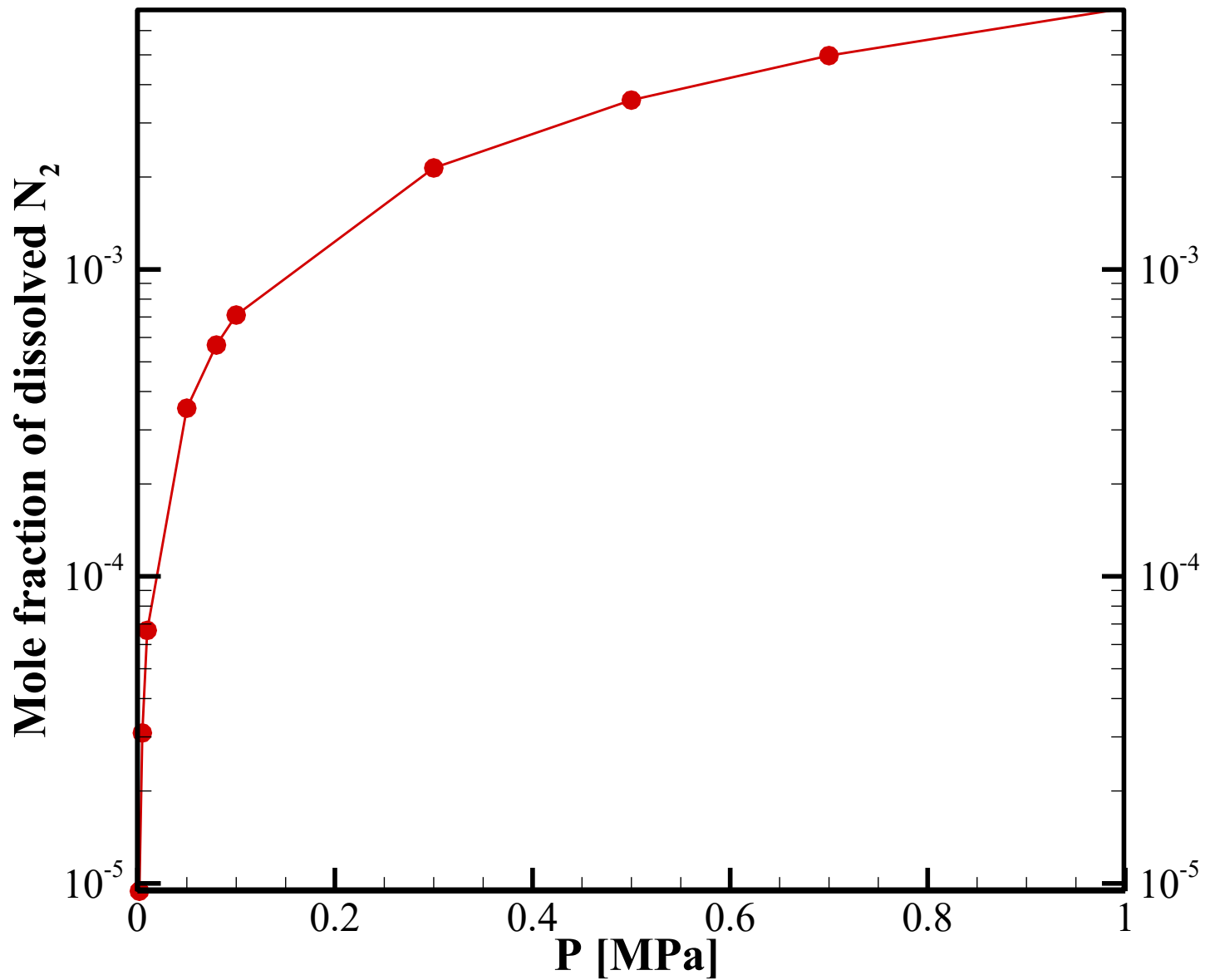
# Non-degassed / degassed





(b)

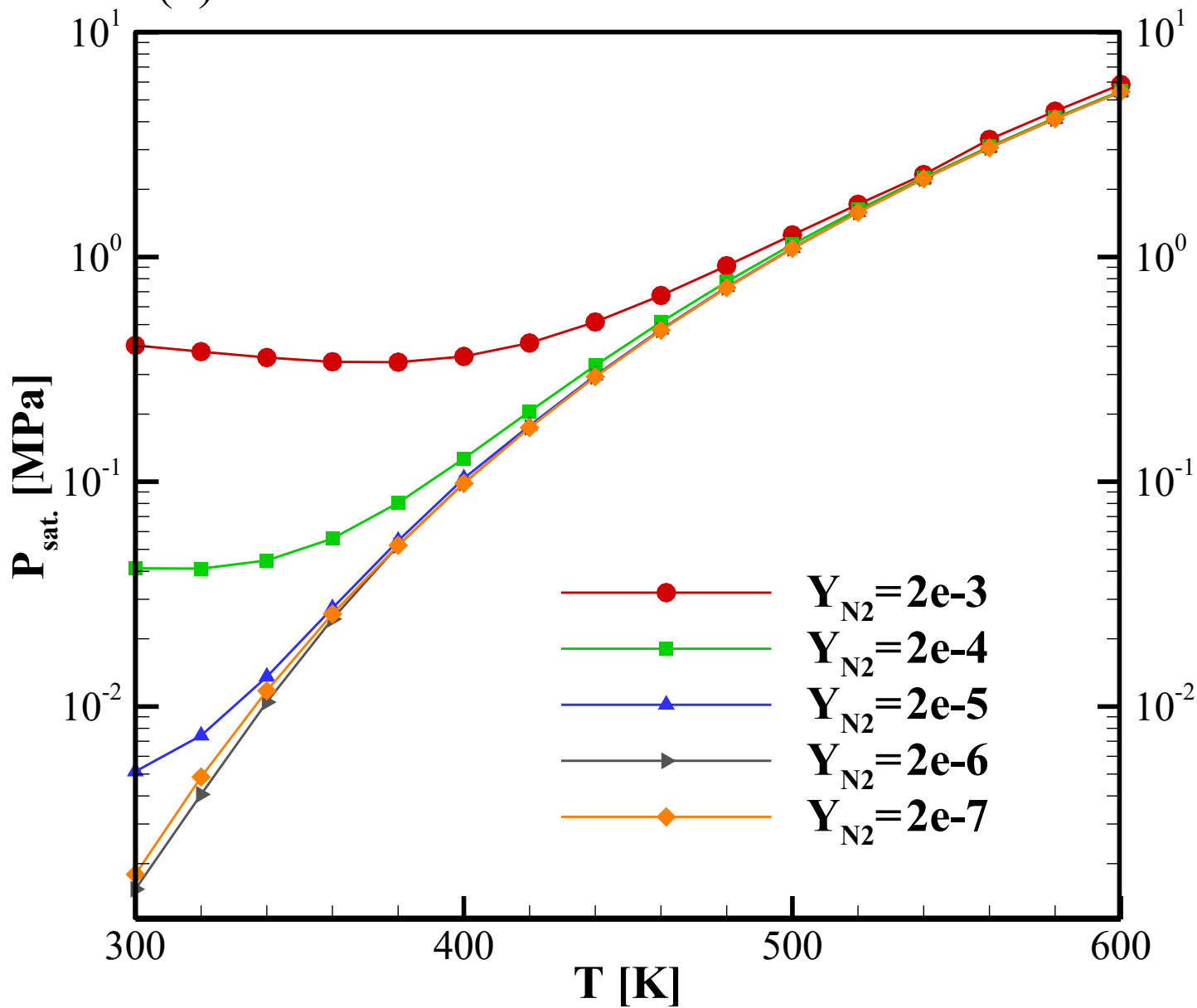
Viscor





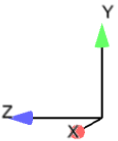
(b)

# Viscor

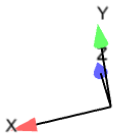
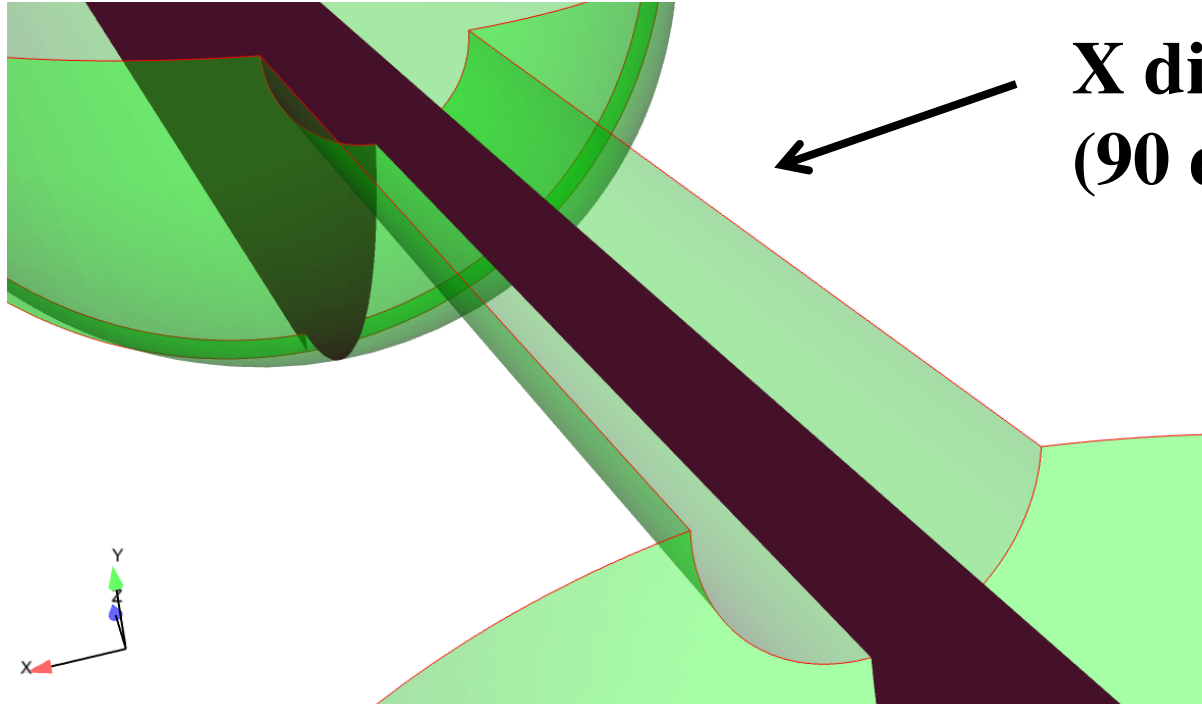




**Y direction  
(0 degree)**



**X direction  
(90 degree)**





**Exp.  
(Non-degas)**

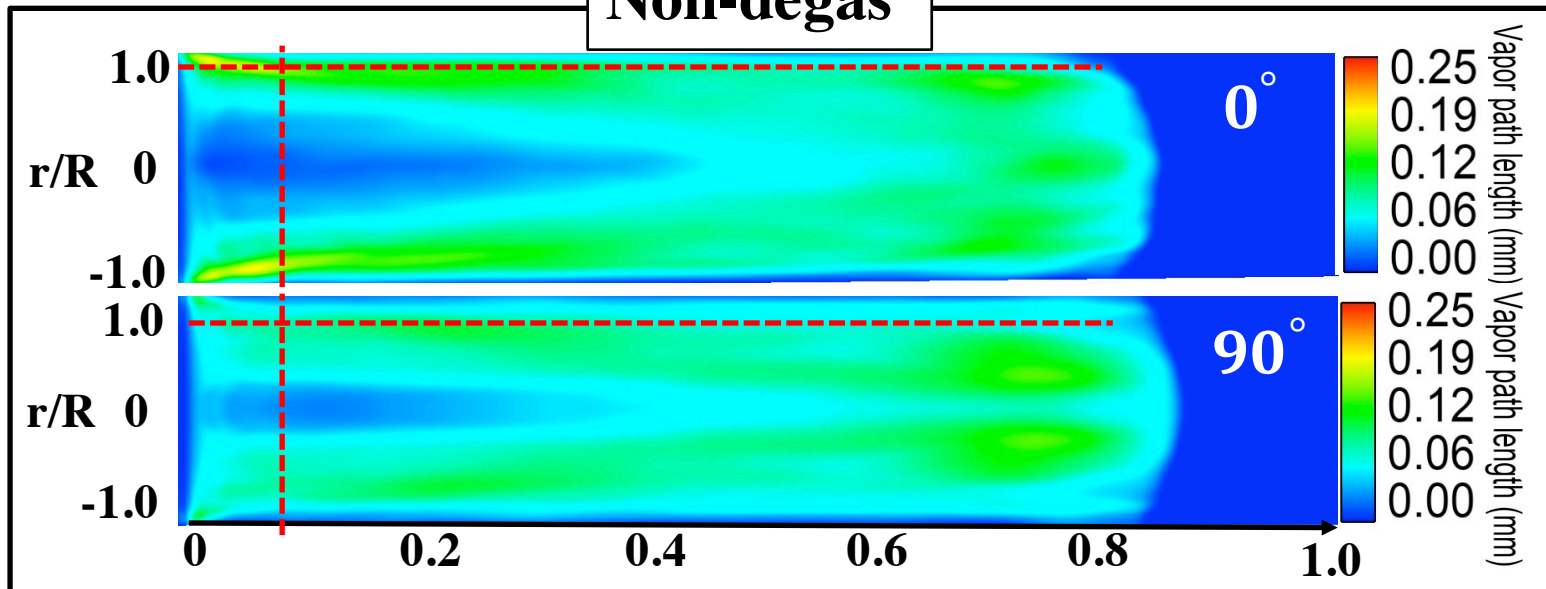


**Exp.  
(Degas)**



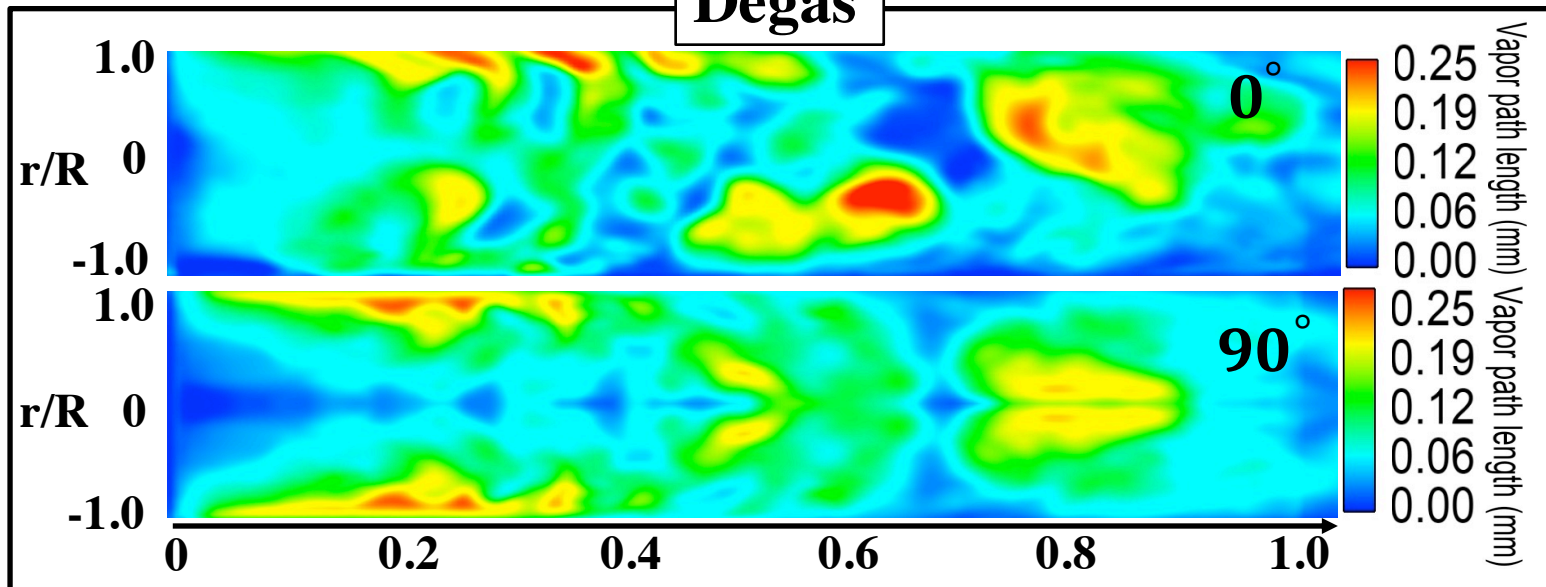
# Non-degas

LES



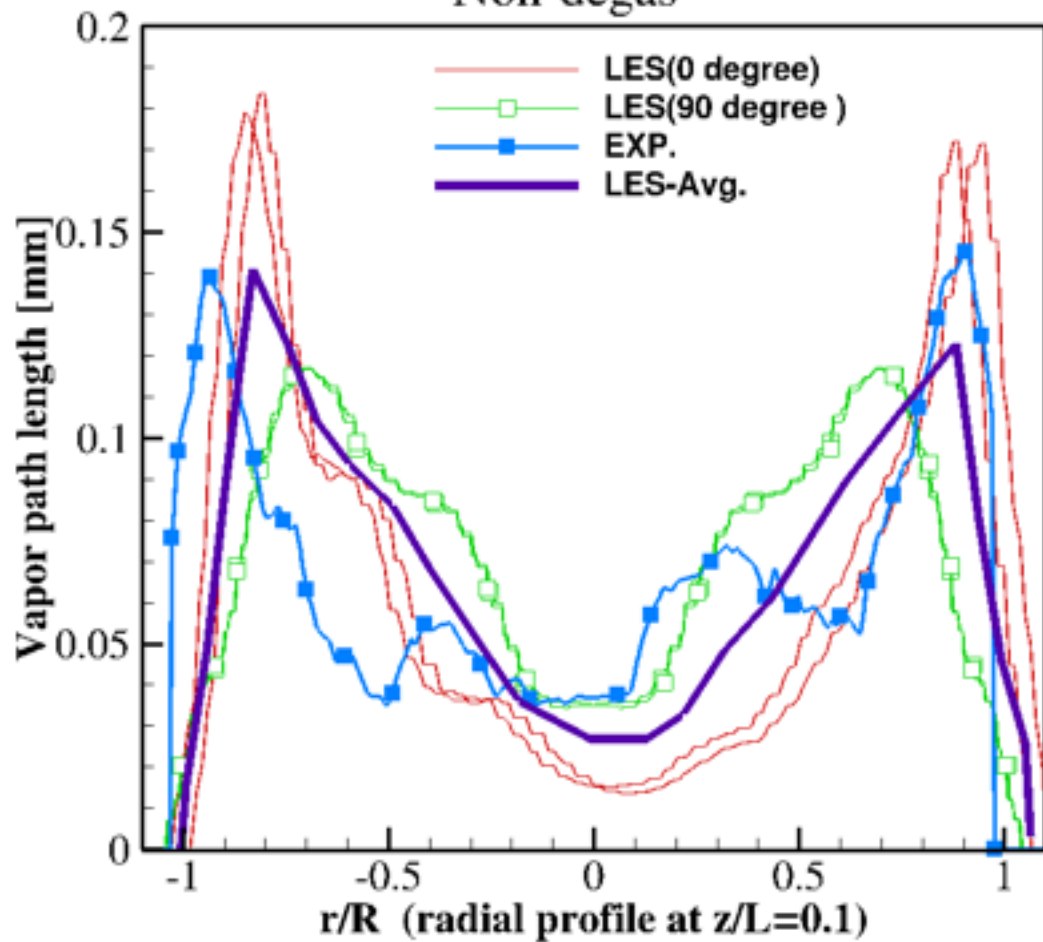
# Degas

LES

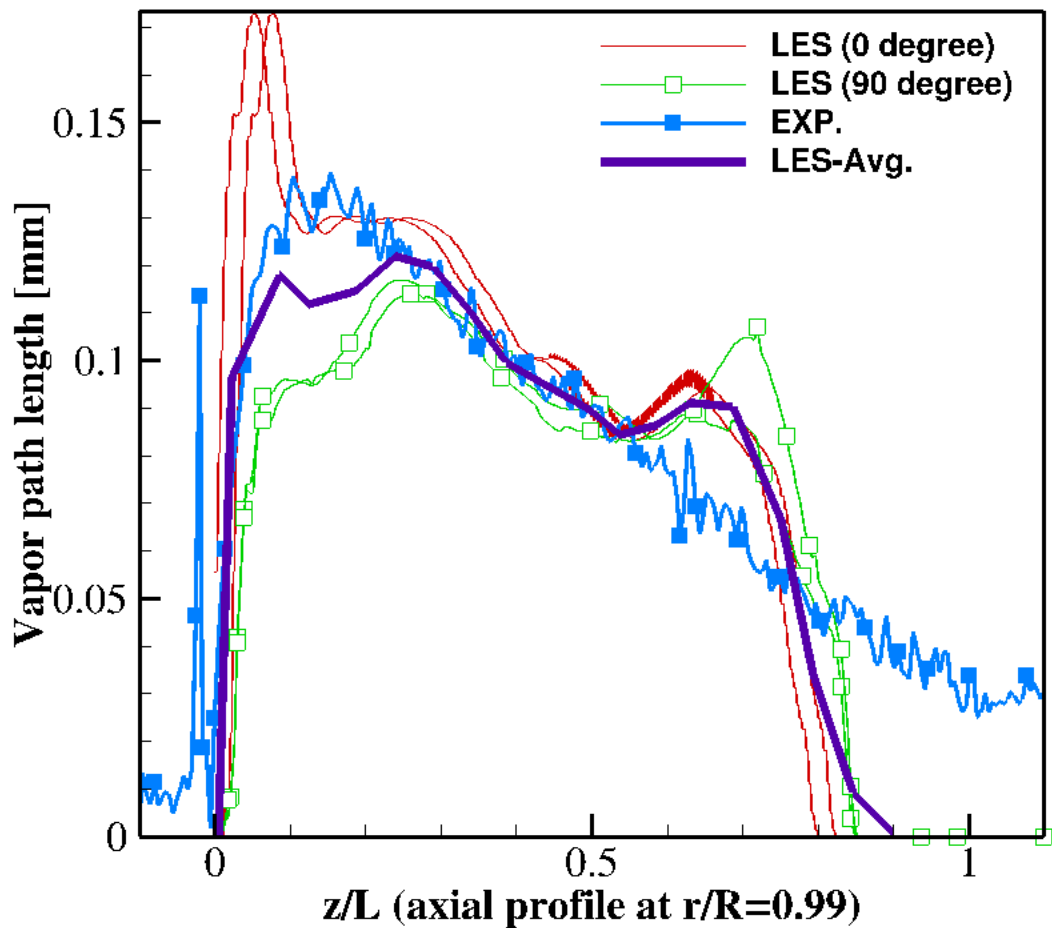


$z/L$

# Non-degas



# Non-degas



$Y_{n2} = 2E-5$

P [Pa]

2.41e+05

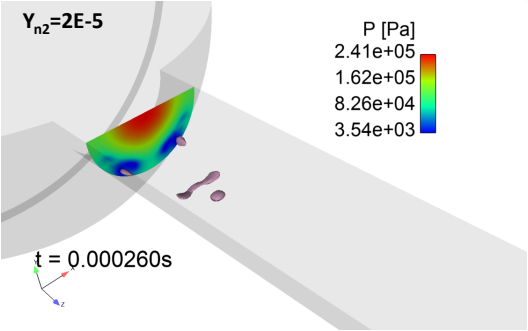
1.62e+05

8.26e+04

3.54e+03



$t = 0.000260s$




P [Pa]

7.83e+04

5.31e+04

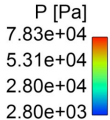
2.80e+04

2.80e+03

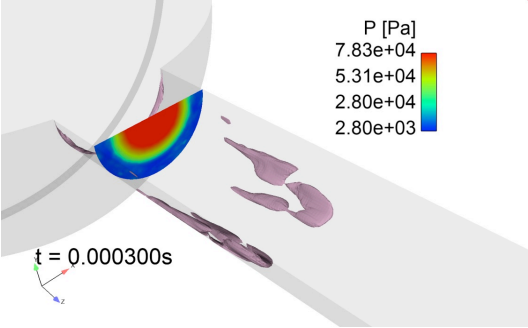


$t = 0.000280s$






$t = 0.000300s$



$Y_{n_2} = 2E-6$

P [Pa]  
1.92e+05  
1.28e+05  
6.52e+04  
2.01e+03



$t = 0.000310s$






P [Pa]

1.50e+05

1.01e+05

5.14e+04


1.98e+03



$t = 0.000330s$



P [Pa]  
9.15e+04  
6.15e+04  
3.15e+04  
1.53e+03



$t = 0.000350s$



$Y_{n_2} = 2E-5$

V [m/s]



t = 0.000260s



$Y_{n_2} = 2E-6$

V [m/s]

53

40

26

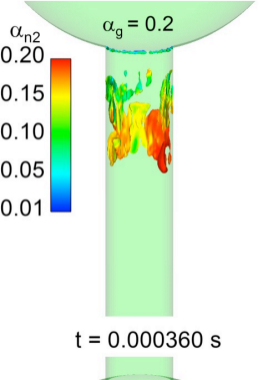
13

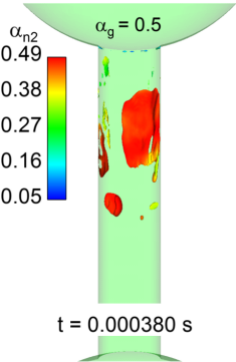
0

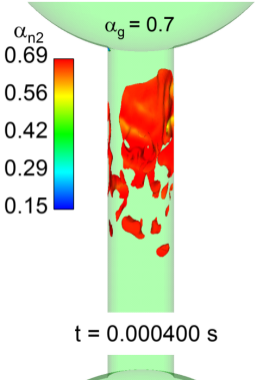


t = 0.000310s









$\alpha_g = 0.9$

$\alpha_{n2}$   
0.90  
0.82  
0.74  
0.67  
0.59



$t = 0.000420$  s

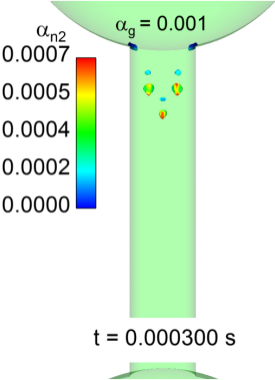


$\alpha_{n2}$   
3.22e-04  
2.50e-04  
1.78e-04  
1.06e-04  
3.39e-05



$\alpha_g = 0.0001$

$t = 0.000280$  s

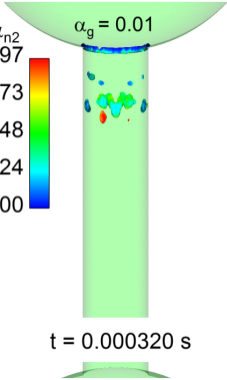


$\alpha_{n2}$   
0.0097  
0.0073  
0.0048  
0.0024  
0.0000



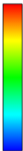
$\alpha_g = 0.01$

$t = 0.000320$  s



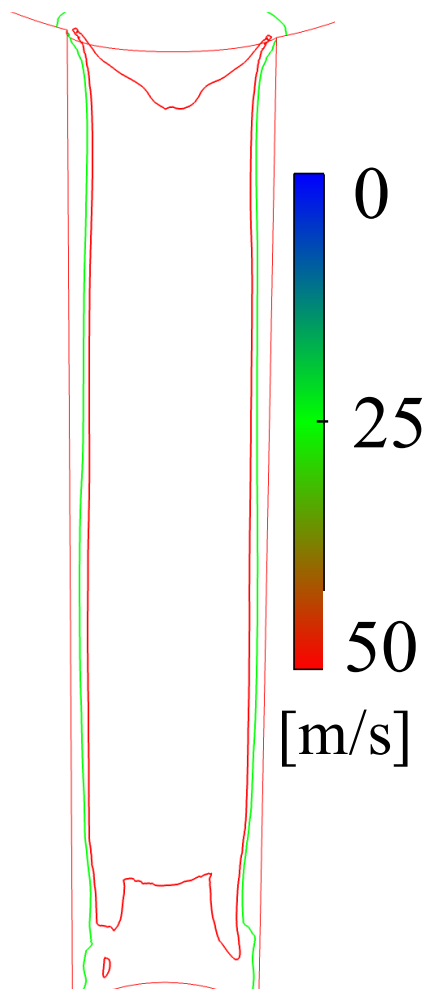
$$\alpha_g = 0.1$$

$\alpha_{n2}$   
0.10  
0.07  
0.05  
0.02  
0.00

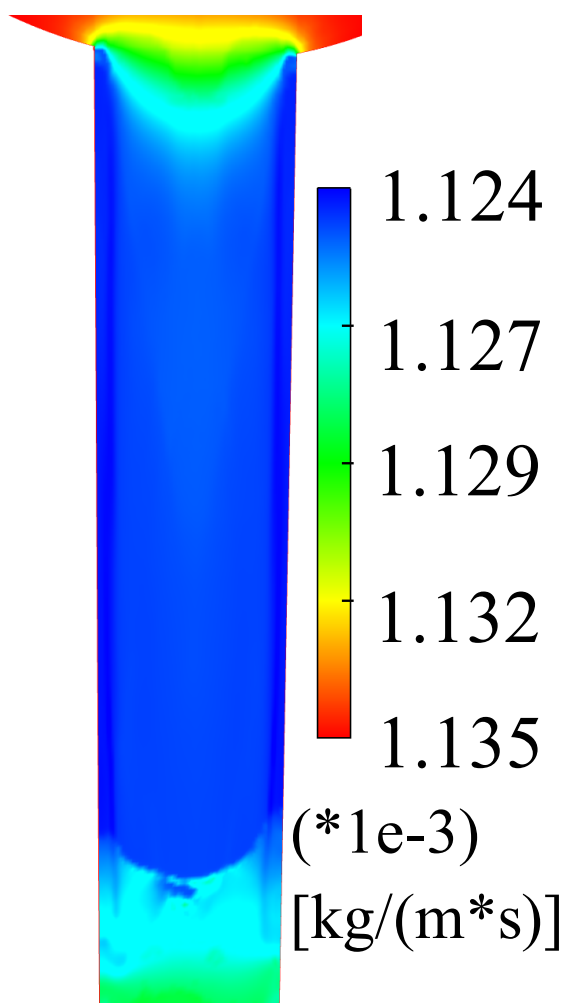


$t = 0.000340$  s

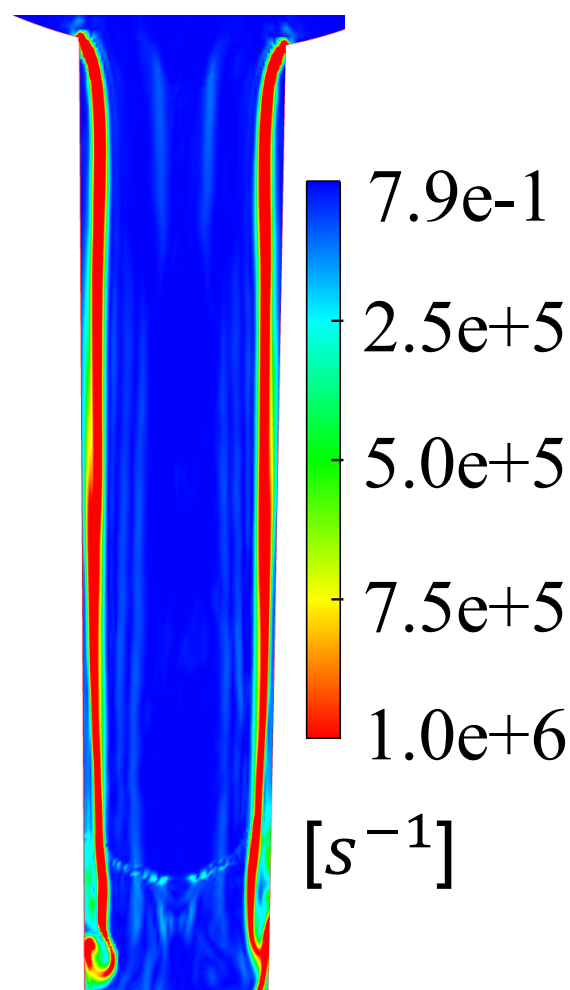




$V$

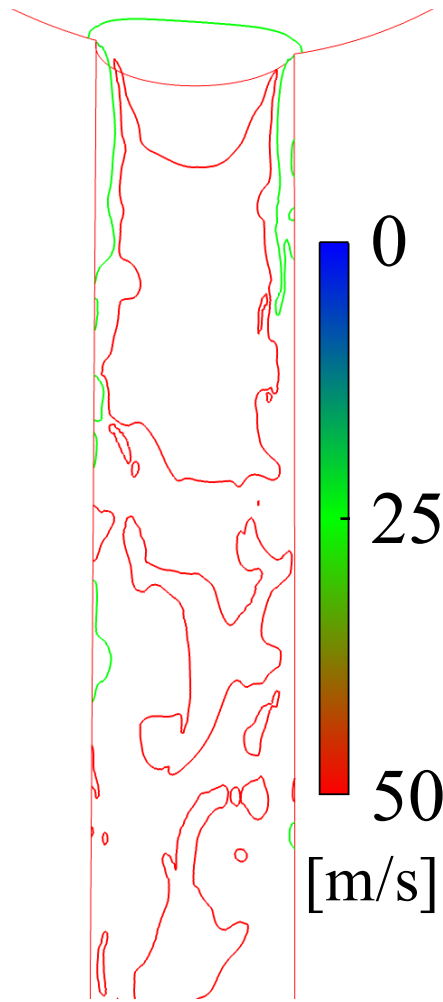


$\mu$

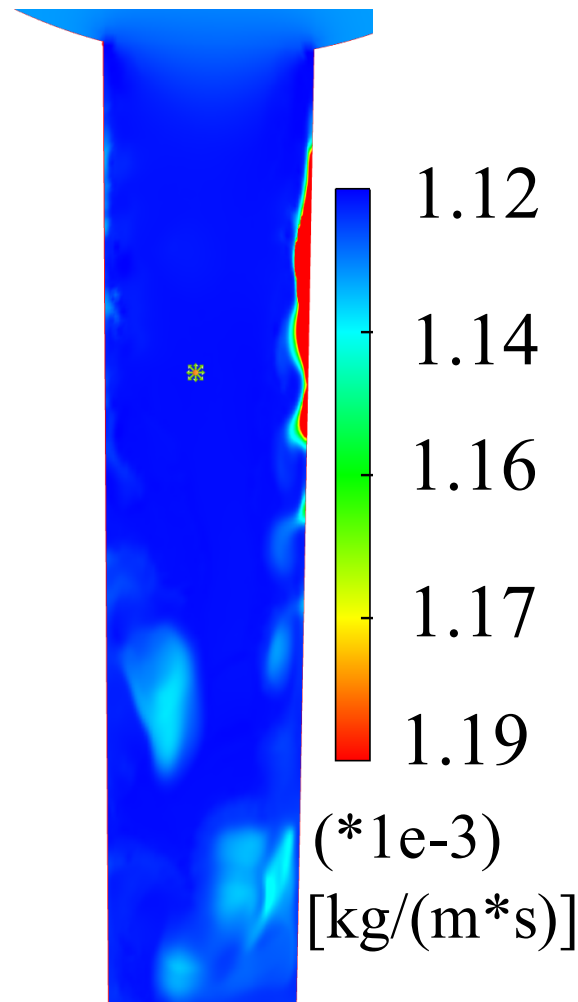


$\omega$

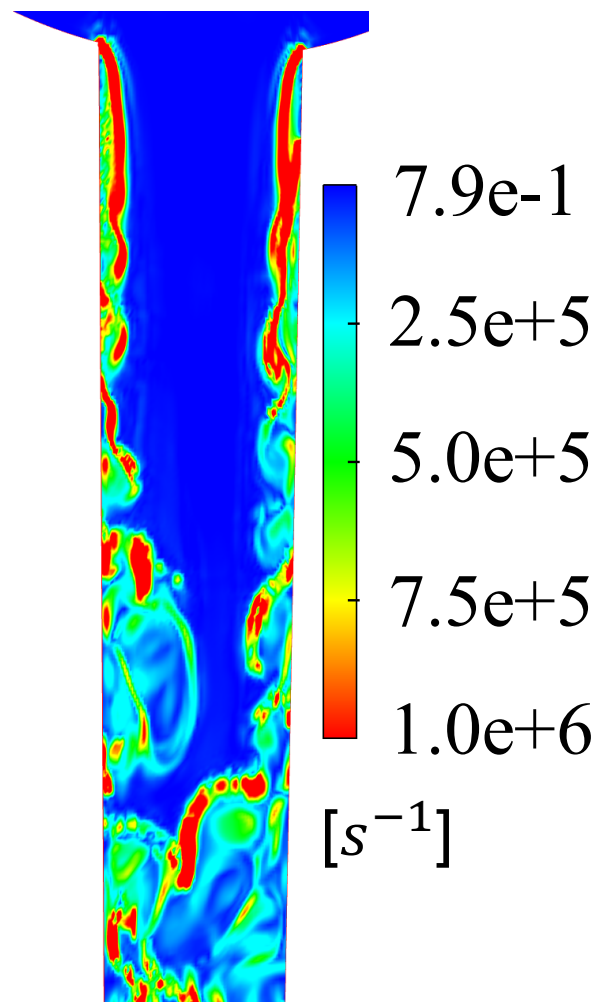
Non-Degassed



$V$

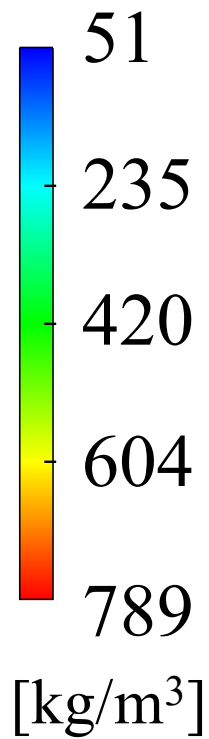
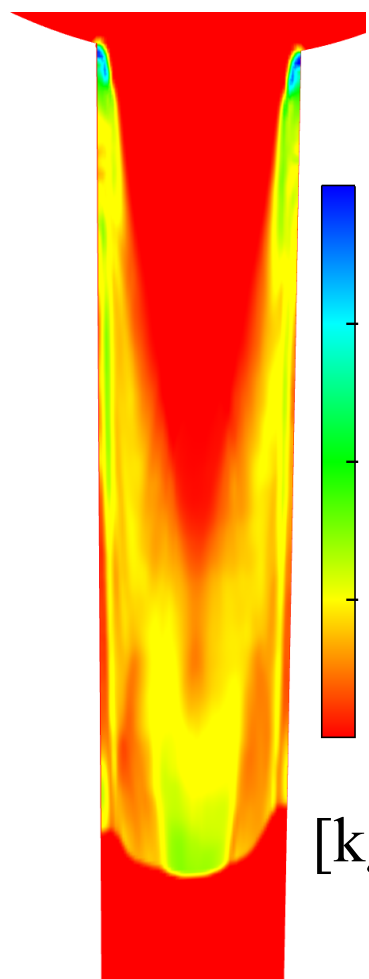


$\mu$

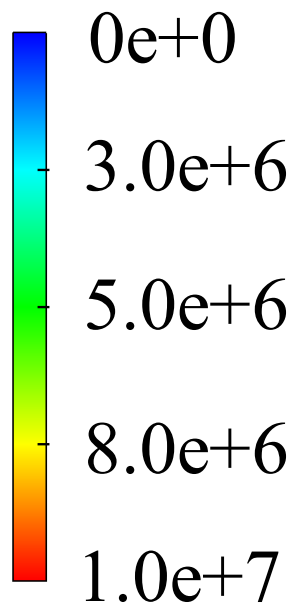
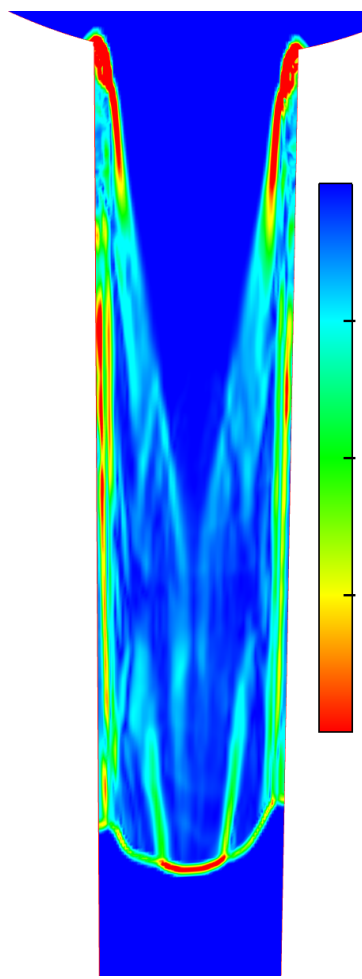


$\omega$

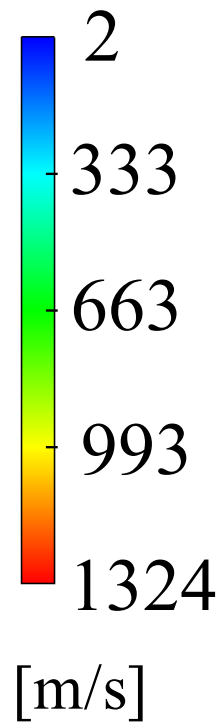
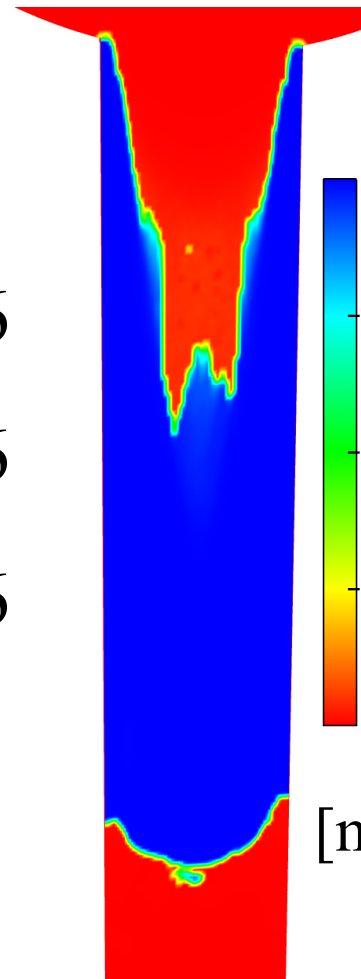
Degassed



$\rho$

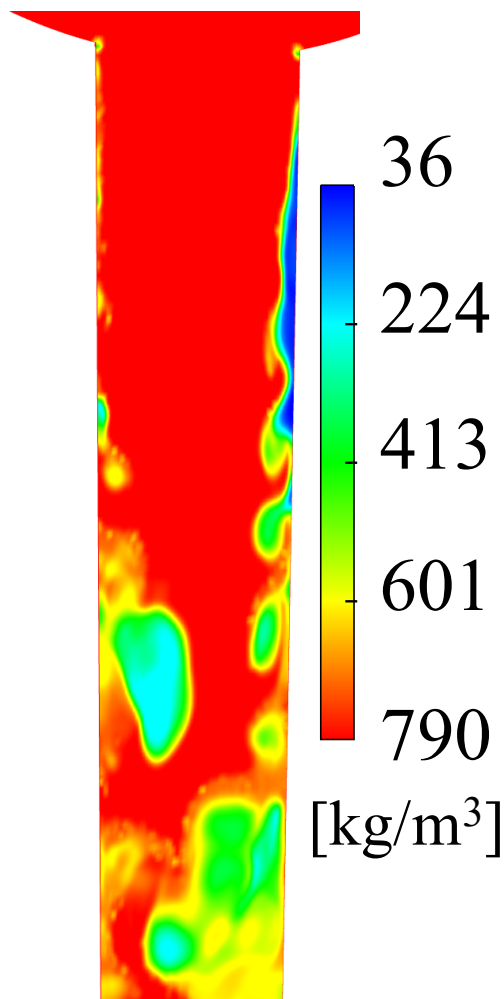


$\nabla\rho$

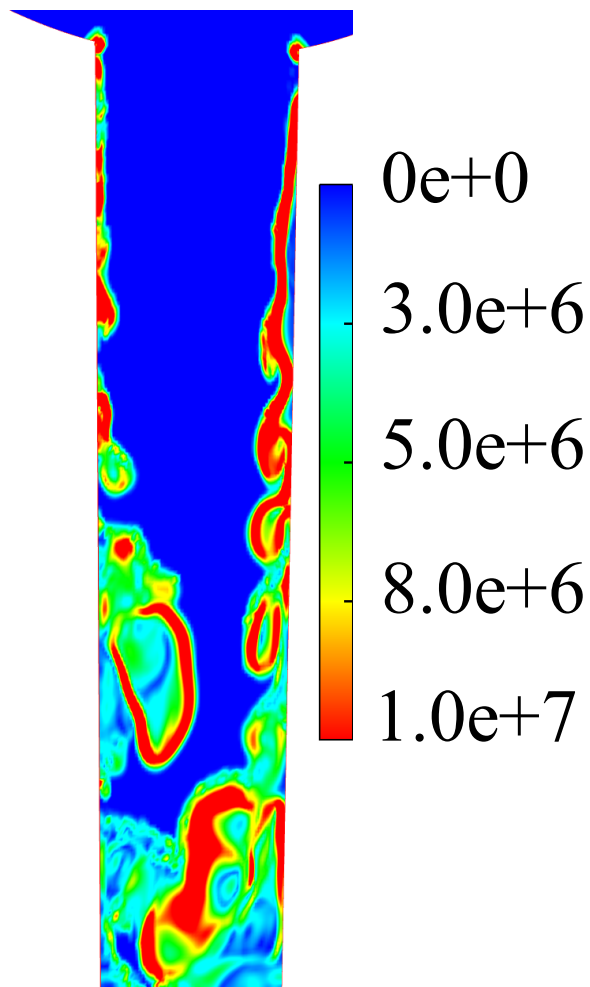


Cs

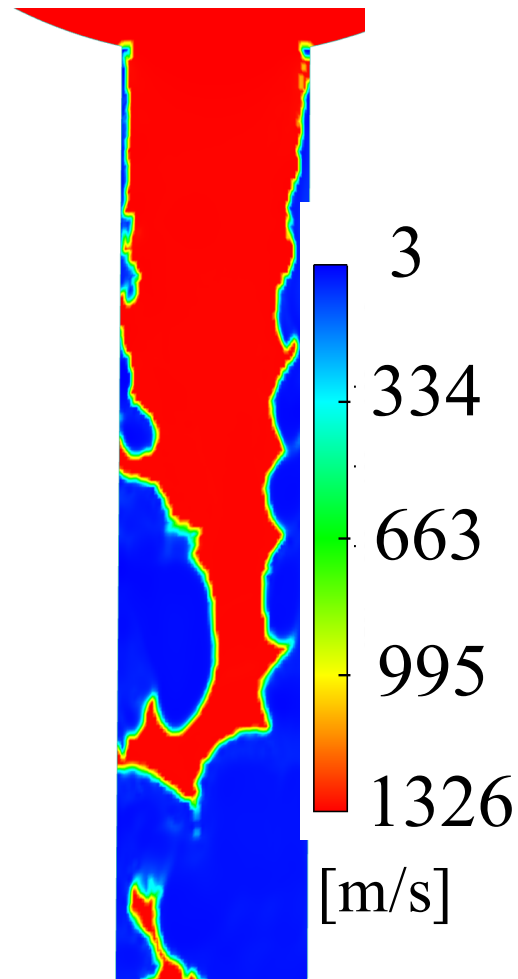
Non-Degassed



$\rho$



$\nabla\rho$



$Cs$

Degassed



